

## Examination of Gravity Waves Associated with the 13 March 2003 Bow Echo

REBECCA D. ADAMS-SELIN\* AND RICHARD H. JOHNSON

*Department of Atmospheric Science, Colorado State University, Fort Collins, Colorado*

(Manuscript received 1 December 2012, in final form 25 April 2013)

### ABSTRACT

Numerical simulations of the 13 March 2003 bow echo over Oklahoma are used to evaluate bow echo development and its relationship with gravity wave generation. Multiple fast-moving (with speeds of 30–35 m s<sup>-1</sup>) gravity waves are generated in association with fluctuations in the first vertical mode of heating in the convective line. The surface impacts of four such waves are observed in Oklahoma Mesonet data during this case. Observations of surface pressure surges ahead of convective lines prior to the bowing process are reproduced; a slower gravity wave produced in the simulation is responsible for a prebowing pressure surge. This slower gravity wave, moving at approximately 11 m s<sup>-1</sup>, is generated by an increase in low-level microphysical cooling associated with an increase in rear-to-front flow and low-level downdrafts shortly before bowing. The wave moves ahead of the convective line and is manifested at the surface by a positive pressure surge. The pattern of low-level vertical motion associated with this wave, in conjunction with higher-frequency gravity waves generated by multicellularity of the convective line, increases the immediate presystem CAPE by approximately 250 J kg<sup>-1</sup> just ahead of the bowing segment of the convective line. Increased presystem CAPE aids convective updraft strength in that segment despite amplified updraft tilt due to a stronger cold pool and surface-based rear-to-front flow, compared to updraft strength in other, nonbowing segments of the convective line.

### 1. Introduction

The ability of convective systems to generate gravity waves is well documented in the literature (Nicholls 1987; Bretherton and Smolarkiewicz 1989; Schmidt and Cotton 1990; Mapes 1993; Fovell 2002; Fovell et al. 2006; Knupp 2006). Specifically, changes in heating and cooling rates in the atmosphere, as are often found with convection, can result in the generation of gravity waves due to the difference in buoyancy between the convection and the surrounding environment (Bretherton and Smolarkiewicz 1989; Nicholls et al. 1991; Mapes 1993). If the vertical heating profile is a harmonic of the depth of the troposphere, the partial reflection of the wave energy at the tropopause allows hydrostatic waves to propagate horizontally for large distances without the aid of a trapping level other than the tropopause (Nicholls et al. 1991). The label of such a wave is equal to the number of

antinodes in the heating profile that generates it; for example, an  $n = 1$  mode wave is generated by a heating profile that extends throughout the troposphere with its maximum at midlevels.

This type of vertical diabatic heating profile is typical during the formation of a convective line given the latent heat release from condensation, freezing, and deposition in the updraft (Houze 1982; Johnson and Young 1983; Gallus and Johnson 1991). The speed of these low-frequency waves is given by

$$c = \frac{NH}{n\pi}, \quad (1)$$

where  $N$  is the Brunt–Väisälä frequency,  $H$  is the vertical depth of the atmosphere, and  $n$  is the vertical mode of the heating profile (Nicholls et al. 1991). In this study, the  $N$  used is the  $N_m$  defined in Bryan and Rotunno (2009). For subsaturated air,  $N_m$  is defined as

$$\left(\frac{g}{\theta_v}\right) \frac{\partial \theta_v}{\partial z}, \quad (2)$$

where  $g$  is gravitational acceleration,  $z$  is height,  $\theta_v = \theta(1 + q_v R_v/R_d)/(1 + q_v + q_l)$ ,  $q_v$  and  $q_l$  are the water vapor and liquid water mixing ratios, and  $R_d$  and  $R_v$  are the gas

\* Current affiliation: Atmospheric and Environmental Research, Inc., Lexington, Massachusetts.

Corresponding author address: Rebecca D. Adams-Selin, HQ Air Force Weather Agency 16th Weather Squadron, 101 Nelson Dr., Offutt AFB, NE 68113.  
E-mail: rebecca.selin.ctr@offutt.af.mil

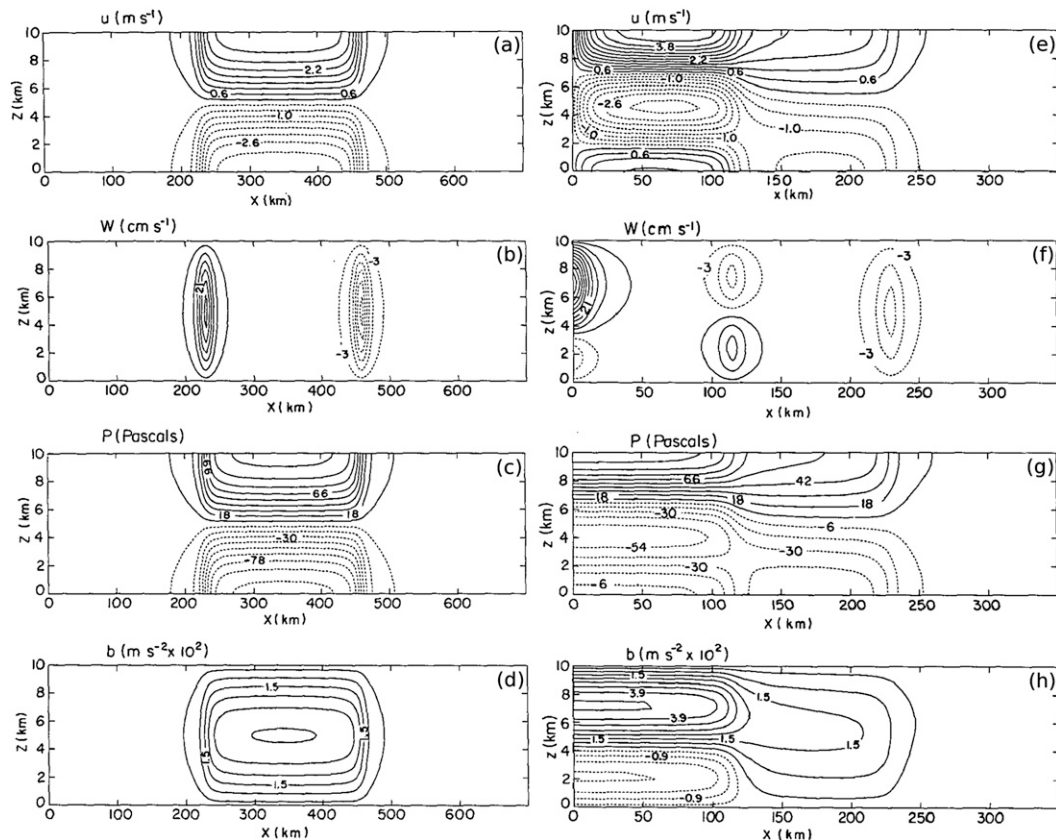


FIG. 1. Signal of a  $2.0 \text{ J kg}^{-1} \text{ s}^{-1}$  convective ( $n = 1$ ) heating pulse underneath a rigid lid at 10 km. The time is 4 h after start of heating; the heating was turned on initially and then turned off after 2 h: (a) horizontal velocity ( $0.3 \text{ m s}^{-1}$ , negative dashed), (b) vertical velocity ( $3 \text{ cm s}^{-1}$ , negative dashed), (c) perturbation pressure (12 Pa; negative dashed), and (d) perturbation buoyancy ( $0.005 \text{ m s}^{-2}$ ). The heating source is at  $x = 0 \text{ km}$ . (e)–(h) As in (a)–(d), but the heating source is the combined  $n = 1$  and  $n = 2$  heating modes, of magnitude  $1.0 \text{ J kg}^{-1} \text{ s}^{-1}$ , and is not turned off. The time is 2 h after start of heating. Adapted from Figs. 10 and 5 of Nicholls et al. (1991).

constants for dry air and water vapor, respectively. The full description of  $N_m$  for saturated air is given in Bryan and Rotunno (2009). Typical values of  $N$  ( $0.01 \text{ s}^{-1}$ ) and  $H$  (10 km) yield an  $n = 1$  wave speed of approximately  $30 \text{ m s}^{-1}$ .

Nicholls et al. (1991) calculated the linear atmospheric response to the introduction of an  $n = 1$  warming temperature profile (Figs. 1a–d). In that study, the heat source, located at  $x = 0 \text{ km}$ , was turned on immediately at the start of the solution, left on for 2 h, and then turned off. The switch “on” of the heat resulted in a temporary low (high) pressure perturbation at the surface (aloft), along with an increase in the  $u$  wind flow toward the heating source at lower levels, and away from the heating source at upper levels [at  $x = 450 \text{ km}$  in Figs. 1a and 1c, also noted by Mapes (1993)]. An increase in potential temperature particularly at midlevels also occurs, generated by subsidence throughout the column following passage of the first wave front (Figs. 1b,d). At the surface, this appears as a temporary decrease in

pressure unaccompanied by a change in temperature. When the heating ceases, a second signal travels at the same speed away from the system. This second response contains ascent throughout the column, and the pressure, potential temperature, and  $u$  wind fields return to the ambient values (Figs. 1a–d at  $x = 225 \text{ km}$ ).

Within the idealized analytical solution of Nicholls et al. (1991), the ambient environment returns to its initial state after both responses pass. However, it was noted by Mapes (1993) that the prestorm environment is in a sense permanently modified with respect to the convective system, as the second response does not appear until the system, and its associated heating, dissipates. The subsidence-induced slight warming and drying throughout the depth of the atmosphere resulting from the first response is a permanent modification, particularly in the midlevels.

The heating profile generated by a system’s stratiform precipitation region, of  $n = 2$  or even  $n = 3$  structures

consisting partially of cooling in low levels, can generate yet another low-frequency gravity wave (Nicholls et al. 1991; Mapes 1993; Lane and Reeder 2001; Fovell 2002; Fovell et al. 2006). In the  $n = 2$  wave, upward (downward) motion is excited on the leading edge of the wave throughout the lower (upper) half of the troposphere; the lower half of the troposphere is adiabatically cooled (Figs. 1f and 1h at approximately  $x = 120$  km display the combined  $n = 1$  and 2 wave responses). The wind profile is modified to create midtropospheric inflow (Fig. 1e; Fovell 2002); a midtropospheric low pressure perturbation is created as well, with high pressure perturbations generated in the lowest and highest third of the troposphere (Fig. 1g). Through (1), it can be seen that this wave moves at half the speed of the  $n = 1$  wave. Pandya and Durran (1996) and Pandya et al. (2000) found that the wind perturbations generated by the combination of  $n = 1$  and 2 gravity waves could largely explain the circulations within a squall line, including the onset of rear-to-front flow.

The  $n = 3$  wave also exhibits a lifting and cooling response on its leading edge, but over the lowest one-third of the atmosphere (Lane and Reeder 2001). The  $n = 3$  cooling profile is typically associated with the onset of melting contributing to a low-level cooling maximum. While both  $n = 2$  and  $n = 3$  wave modes cool and moisten the lower levels, Lane and Reeder (2001) found that the  $n = 3$  wave had a more significant effect in decreasing the prestorm environment convective inhibition (CIN). This is because the peak upward vertical motions associated with this wave were located lower, closer to the subcloud layer, a major determinant of CIN. Combinations of the  $n = 2$  and  $n = 3$  waves can act as positive feedbacks to their generating systems, cooling and moistening the lower-level air feeding into the storm and organizing surrounding convection (Schmidt and Cotton 1990; Mapes 1993; McAnelly et al. 1997; Lane and Reeder 2001; Fovell 2002; Fovell et al. 2006; Lane and Moncrieff 2008; Bryan and Parker 2010; Lane and Zhang 2011).

Heating profiles that are not harmonics of the depth of the troposphere also generate gravity wave responses similar in appearance to those discussed above. With reduced opportunity for reflection these waves can propagate vertically out of the troposphere more quickly, but that is not always the case: gravity wave responses to low-level cooling were produced in Parker (2008) and Schumacher (2009) that remained near the surface. In idealized linear simulations, Haertel and Johnson (2000, hereafter HJ00) found that the gravity wave response to cooling over the lowest 4 km of the troposphere results in a prominent pressure signal at the surface 6 h into the simulation. This response was in addition to the features

associated with the gravity current that was also generated. Furthermore, if the cooling source moves at a speed approximately equal to that of its generated wave, the wave response is amplified. For example, the positive surface pressure perturbation was from 20% to 35% larger in magnitude when the cooling source moved at a speed close to the gravity wave speed as opposed to remaining stationary.

Finally, Fovell et al. (2006) noted that high-frequency nonhydrostatic gravity waves propagating in the troposphere ahead of a squall line can be generated by multicellular development and frequent temporal changes of the heating profile within a convective line. These waves do require a trapping layer to not quickly propagate out of the troposphere; the curvature of the wind profile due to outflow aloft from the system at anvil level can provide this. They found that small amounts of water condensed within the updrafts associated with these high-frequency waves, increasing the parcel's buoyancy, and small clouds formed. This particularly can occur if the lower levels have previously been lifted, cooled, and moistened by a low-frequency gravity wave. The newly formed clouds are then advected toward the main system by the system-relative wind. As the clouds are ingested by the system, the increase in buoyancy can act to locally strengthen the convective line, provided the cloud has not already developed rainfall and its own associated cold pool (Fovell et al. 2006).

Few studies have documented real-world observations of hydrostatic waves. Bryan and Parker (2010) observed buoyancy and pressure patterns in conjunction with an Oklahoma squall line that appeared to be an  $n = 1$  gravity wave. Adams-Selin and Johnson (2010, hereafter ASJ10) noted surface pressure and temperature patterns associated with an Oklahoma bow echo that appeared to correspond to  $n = 1$  and 2 gravity waves, but because that study only dealt with surface observations, this could not be confirmed. One specific pressure feature observed by ASJ10, a surge of the mesohigh partially ahead of the convective line, appeared in conjunction with new bowing in 35 of 39 bow echoes observed in Oklahoma over the 4-yr ASJ10 study, suggesting a connection to bowing development.

Thus, the goal of this study is to determine if the surface pressure features noted in ASJ10 were indeed generated by gravity waves, and if so to ascertain the effect of those waves on the bow echo system particularly in relation to new bowing development. An idealized, high-resolution cloud model 1 simulation (CM1; Bryan and Fritsch 2002) will be used to reproduce these pressure features and their cause. A discussion of the bow echo, which occurred on 13 March 2003, and all observed pressure features is given in section 2. The CM1 model

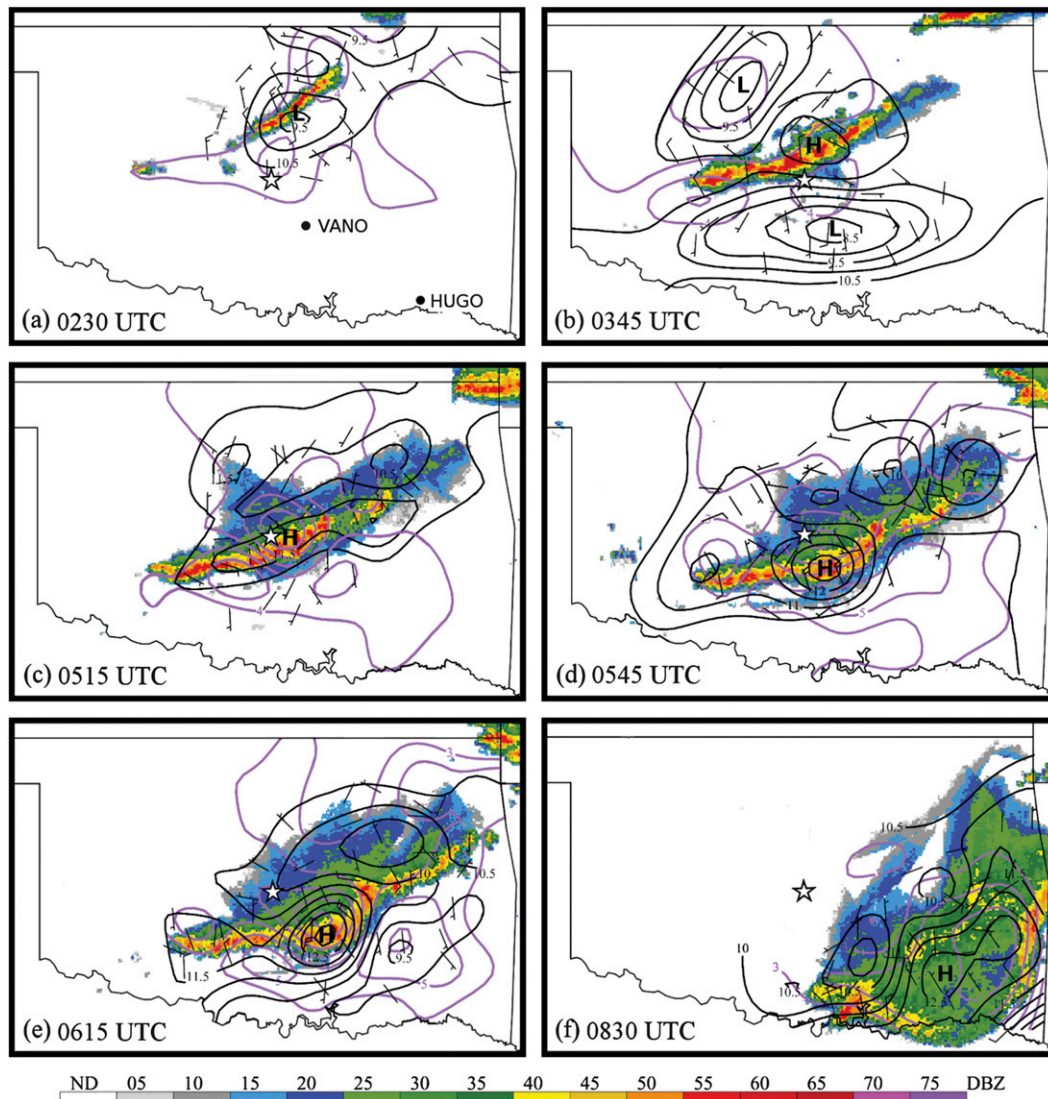


FIG. 2. WSI NOWrad base reflectivity from (a) 0230, (b) 0345, (c) 0515, (d) 0545, (e) 0615, and (f) 0830 UTC 13 Mar 2003. High-pass filtered potential temperature (purple,  $1^{\circ}\text{C}$ ), surface wind (black, barbs), and adjusted pressure (black, 0.5 hPa). High and low pressure maxima are denoted by letters H and L respectively. The star is the KTLX radar, and the black dots in (a) are the Oklahoma Mesonet stations VANO and HUGO. (From ASJ10.)

used is described in section 3. Sections 4 and 5 analyze the low-frequency wave features simulated in the CM1 model, and section 6 discusses the high-frequency wave features seen. Section 7 provides the conclusions.

## 2. 13 March 2003 case review

### a. Fast-moving low pressure perturbations

Figure 2, adapted from ASJ10, displays composite Weather Services International National Operational Weather Radar (WSI NOWrad) reflectivity data, overlaid with high-pass Lanczos-filtered pressure and temperature

data from the Oklahoma Mesonet. (The high-pass filtering was designed to remove synoptic features from the data; see ASJ10 for more details.) The 13 March 2003 bow echo initialized as a convective line in central Oklahoma, in isolation from other convection at 0230 UTC (Fig. 2a). A low pressure region was evident centered over the convective line. This low pressure region quickly split and propagated away from the convective line (0345 UTC; Fig. 2b).

Data time series from Oklahoma Mesonet stations VANO and HUGO, the locations of which are shown by black dots in Fig. 2a, are given in Fig. 3. A dip in pressure, unaccompanied by a temperature change, is shown

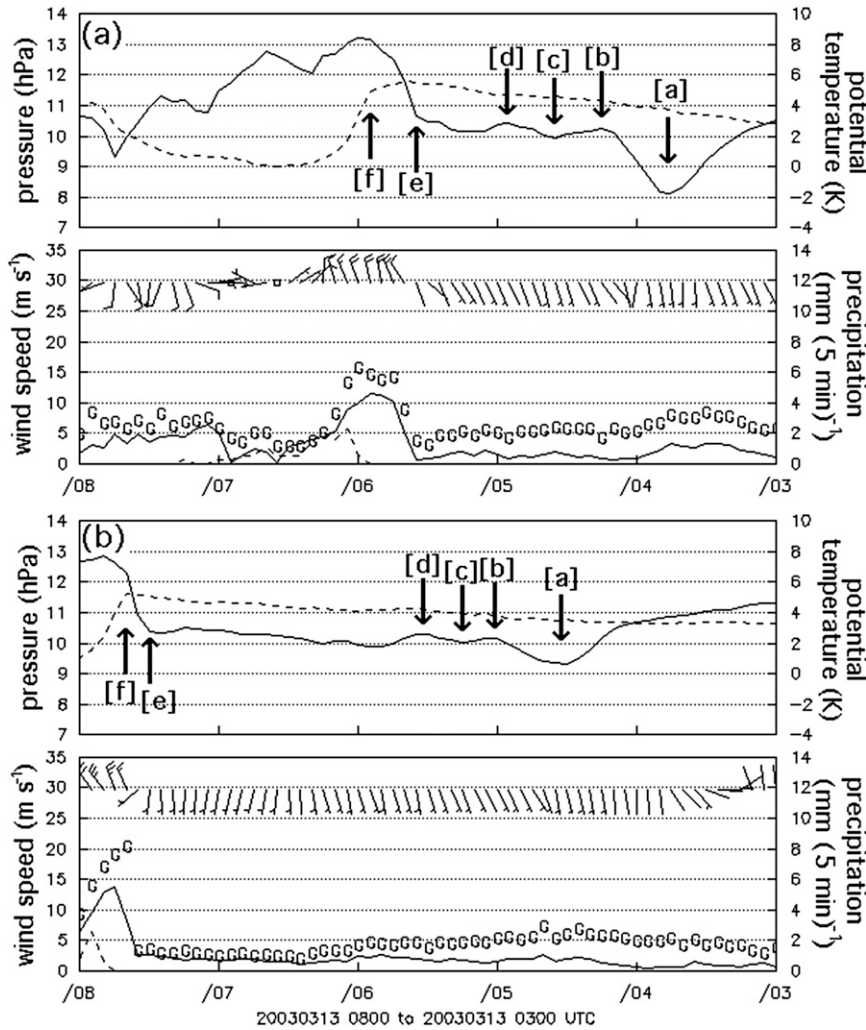


FIG. 3. Time series display of high-pass filtered data from stations (a) VANO and (b) HUGO from the Oklahoma Mesonet (locations shown in Fig. 2a). Time increases from the left from 0300 to 0800 UTC 13 Mar 2003. Upper graphs in each figure show potential temperature (K, dashed, upper-right scale) and adjusted pressure (hPa, solid line, upper-left scale). Lower graphs show sustained winds (kt, barbs,  $1 \text{ kt} = 0.5144 \text{ m s}^{-1}$ ), sustained wind speed ( $\text{m s}^{-1}$ , solid line, lower-left scale), unfiltered wind gusts ( $\text{m s}^{-1}$ , displayed as “G”, lower-left scale), and unfiltered precipitation rate [ $\text{mm (5 min)}^{-1}$ , dashed line, lower-right scale]. Arrows a–f refer to indications of passing gravity waves or gravity current at each station and are referenced in the text.

at arrow a at both stations. This would seem to be indicative of an  $n = 1$  gravity wave feature, as discussed above. In ASJ10, this dip in pressure was tracked in numerous Mesonet stations across Oklahoma, and an average ground-relative speed of  $34.1 \text{ m s}^{-1}$  was calculated. Isochrones of this feature are displayed in Fig. 4a. The mean environmental tropospheric wind speed parallel to the direction of motion of the feature,  $1.6 \text{ m s}^{-1}$ , was computed using the 0000 UTC sounding from Norman, Oklahoma (KOUN; Fig. 5). Accounting for this tailwind yielded an actual feature speed of  $32.5 \text{ m s}^{-1}$ .

Upon further examination of these time series, additional pressure features, also possibly indicative of gravity waves, were noted. Because these features are such small variations in pressure, they did not appear in the objective analysis. However, in Fig. 3, arrows b, c, and d at each station are also pressure rises and dips unaccompanied by surface temperature changes. These features were evident at multiple Mesonet stations across Oklahoma as well, and isochrones of each feature are shown in Figs. 4b–d. The ground-relative speeds of these features are estimated to be 32.8, 28.3, and

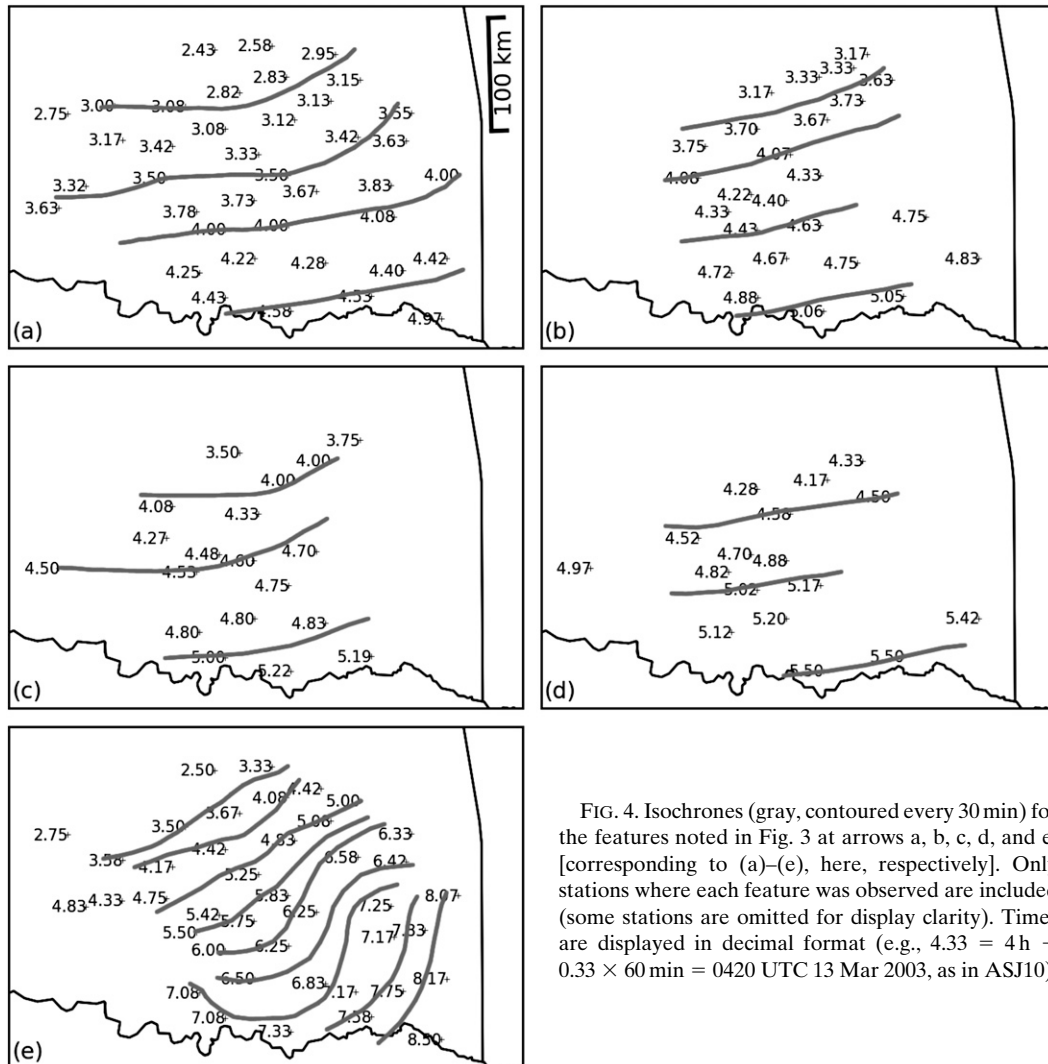


FIG. 4. Isochrones (gray, contoured every 30 min) for the features noted in Fig. 3 at arrows a, b, c, d, and e, [corresponding to (a)–(e), here, respectively]. Only stations where each feature was observed are included (some stations are omitted for display clarity). Times are displayed in decimal format (e.g., 4.33 = 4 h + 0.33 × 60 min = 0420 UTC 13 Mar 2003, as in ASJ10).

$35.5 \text{ m s}^{-1}$ , which are very similar to the ground-relative speed of the initial feature denoted by arrow a, particularly considering the possible errors inherent in the estimation.

As discussed above, Nicholls et al. (1991) noted that upon the decrease of the amplitude of an  $n = 1$  heating profile, a positive pressure perturbation propagates quickly away from the heating source in the lower half of the troposphere. Thus, it is possible that the low pressure perturbations indicated by arrows a and c were gravity waves generated by a sudden increase in the amplitude of an  $n = 1$  heating profile, and the pressure increases at arrows b and d signatures of a sudden decrease in that profile. The large magnitude of the pressure response at arrow a could have resulted from the larger initial increase in convective heating as the updraft first developed. However, without observations of the heating

profile within the convective system, such suppositions cannot be validated.

Bryan and Parker (2010) observed similar oscillations in surface pressure prior to passage of a squall line. They related the initial oscillation in surface pressure to the combination of an approaching cold front and a hydrostatic response to surface cooling by anvil shading. In this case the synoptic features have been removed from the pressure data by the filtering technique, and the anvil had not yet reached the stations when the pressure rises at arrows b and d occurred. Nevertheless, determination of the features as gravity waves requires a numerical model.

#### b. Pressure surge

The second pressure feature associated with the system noted by ASJ10 was a mesohigh surge partially

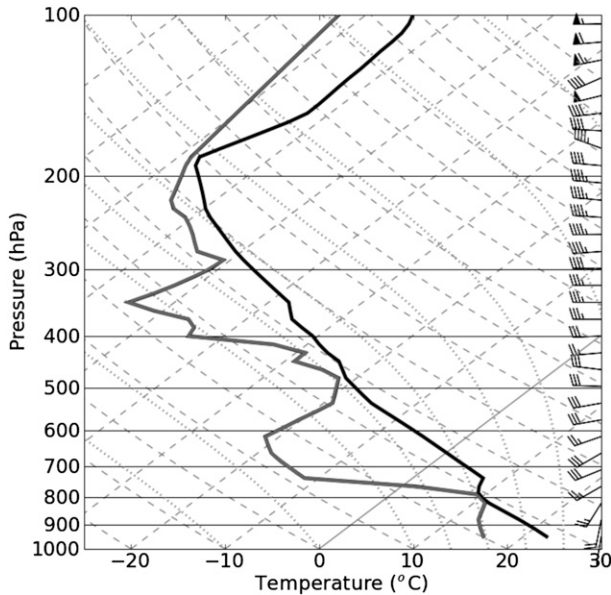


FIG. 5. The 0000 UTC 13 Mar 2003 KOUN sounding, with temperature (black, °C) and dewpoint (gray, °C).

ahead of the convective line. Between 0345 and 0515 UTC (Figs. 2b,c) a mesohigh pressure perturbation formed over the convective line and spread southwestward as the convective intensity strengthened. At 0545 UTC (Fig. 2d) the mesohigh surged partially ahead of the convective line. This was shortly followed by new bowing development within the line at 0615 UTC (Fig. 2e).

It was noted in ASJ10 that the size of the mesohigh pressure surge in this figure produced by the objective analysis was excessive compared to time series observations. Given the pressure surge speed of  $21.6 \text{ m s}^{-1}$  during this time, the distance corresponding to the 20-min interval between the initial pressure rise and final pressure peak at station VANO (arrows e and f in Fig. 3a) should be 25.9 km. However, the pressure interval in Fig. 2d is approximately 60 km. Thus, while the mesohigh surge ahead of the convective line existed, its size was overestimated by about a factor of 2–3. Multiple objective analysis methods were tried in an attempt to fix this overestimation, but it was an inherent problem in all analysis methods.

Figure 3a shows a sharp increase in pressure, a wind shift of almost  $180^\circ$ , and an increase in wind speed all at 0535 UTC (arrow e), but no accompanying potential temperature drop. The sharp temperature drop and onset of rain 20 min later at 0555 UTC (arrow f) indicated the arrival of the surface cold pool or gravity current. This pressure rise, significantly in advance of the temperature drop, occurred at almost all Mesonet stations passed by the bow echo system, including station HUGO (Fig. 3b, arrows e and f.) The ground-relative

speed of the feature was estimated to be  $21.6 \text{ m s}^{-1}$  (ASJ10). If the mean environmental wind speed of  $1.6 \text{ m s}^{-1}$  in the direction of surge motion is accounted for, the actual feature speed is  $20.0 \text{ m s}^{-1}$ .

These observations could be indicative of one of three features: a gravity wave response generated by low-level cooling behind the convective line, similar to simulations in Haertel et al. (2001); a nonhydrostatic pressure response to an intensifying cold pool as in Wakimoto (1982) or Klemp (1994); or a bore propagating ahead of the system in a stable boundary layer as in Parker (2008). Without observations above the surface it is not possible to discriminate among these three possibilities. Thus, a numerical model was used to simulate and evaluate this feature.

### 3. Model description

Cloud model 1 (CM1; Bryan and Fritsch 2002), version 1.15, was initialized with the 0000 UTC 13 March 2003 Norman, Oklahoma (KOUN), sounding, which is shown in Fig. 5. This sounding was released approximately two hours prior to convective initiation, and 100 km to the south. Minor smoothing was performed to remove absolute instabilities and prevent overturning immediately after initialization, and missing moisture data were extrapolated to upper levels, but otherwise the sounding was unmodified. The observed convection formed along a southwest–northeast line approximately  $60^\circ$  clockwise of the north–south direction (Fig. 2a). The wind profile from the sounding was used unmodified in the idealized simulation, but the idealized convection initiated along a south–north line. As a result, the simulated line-normal wind shear values were different than those of the observed convective line. The 0–2.5-km shear in the simulation was  $14 \text{ m s}^{-1}$  instead of the observed  $11.7 \text{ m s}^{-1}$ , and 0–5-km shear was  $14.2 \text{ m s}^{-1}$  instead of  $6 \text{ m s}^{-1}$ .

In a Weather Research and Forecasting Model (WRF) simulation of this case study, the 0–5-km wind shear at KOUN at the time of convective initialization had increased to  $9 \text{ m s}^{-1}$ , suggesting that the environmental shear was increasing after the 0000 UTC sounding. In an idealized simulation with the initial wind direction at each point rotated by  $60^\circ$  counterclockwise so the line-normal shear values were identical to those observed, a bow echo did not form, suggesting shear over a deeper layer may be necessary for formation of an intense convective line as in Stensrud et al. (2005). A discussion of these implications, however, is beyond the scope of this study.

The domain covered 300 km ( $x$  direction) by 200 km ( $y$  direction) by 18 km vertically. A horizontal resolution of 250 m was used with a 2-s time step. The vertical resolution was 100 m from the surface to 4 km aloft; the resolution stretched to 500 m above 8 km. Lateral boundary

conditions were open radiative; lower and upper boundary conditions were zero flux. Vertically implicit Klemp–Wilhelmson time-splitting was used with an acoustic time step of  $1/3$  s. Rayleigh damping was applied above 14 km with an inverse  $e$ -folding time of  $1/300$  s $^{-1}$ . The Thompson et al. (2008) microphysics parameterization and a prognostic turbulent kinetic energy (TKE) subgrid turbulence parameterization (Bryan and Fritsch 2002) were used; radiation and surface flux parameterizations were not included. The domain was translated  $12.5$  m s $^{-1}$  in the  $x$  direction and  $3.3$  m s $^{-1}$  in the  $y$  direction to keep the system inside.

The initialization method was the “cold pool–dam break” (Weisman et al. 1997). In this method, a “cold dam” of air was created along the left side of the domain by decreasing the initial potential temperature. This was done from 0 to 100 km in the  $x$  direction, and 30 to 170 km in the  $y$  direction. The magnitude of the potential temperature perturbation was  $-6$  K at the surface, and linearly decreased until reaching 0 K 2.5 km aloft. As the simulation began, the cold pool dam “broke” and surged forward as a gravity current. Air in advance of the gravity current was forced upward, generating convection.

Coriolis forcing was not included in this simulation. Previous studies have noted that the temperature perturbations generated by gravity waves become trapped within a Rossby deformation radius, dependent upon the speed of the gravity wave (Johnson and Mapes 2001; Liu and Moncrieff 2004). The time and space scales within this study are small enough that this does not affect the results. However, these effects would begin to be noticed when tracking a fast-moving gravity wave over larger spatial scales; for a gravity wave at the latitude of Oklahoma, the Rossby radius of deformation (given as  $\lambda_R = NH/f_c$ , where  $f_c$  is the Coriolis parameter at 35°N latitude and  $H$  is the height of the troposphere, 12 km) would be approximately 1120 km.

#### 4. Multiple $n = 1$ gravity waves

Within the CM1 simulation, convection initializes at 0015 (15 min) simulation time, directly over the edge of the gravity current created by the broken “cold pool dam”. By 0035 cloud water reaches approximately 12 km vertically and remains there for the rest of the simulation. A low pressure perturbation (defined as departure from the initial pressure field) of  $-1$  hPa becomes evident at the lowest model level parallel to and just ahead of the convective line (not shown). By simulation time 0050, this feature has propagated approximately 30 km ahead of the convective line (Fig. 6a) and appears very similar to the observed fast-moving low pressure perturbation noted in Figs. 2a and 2b.

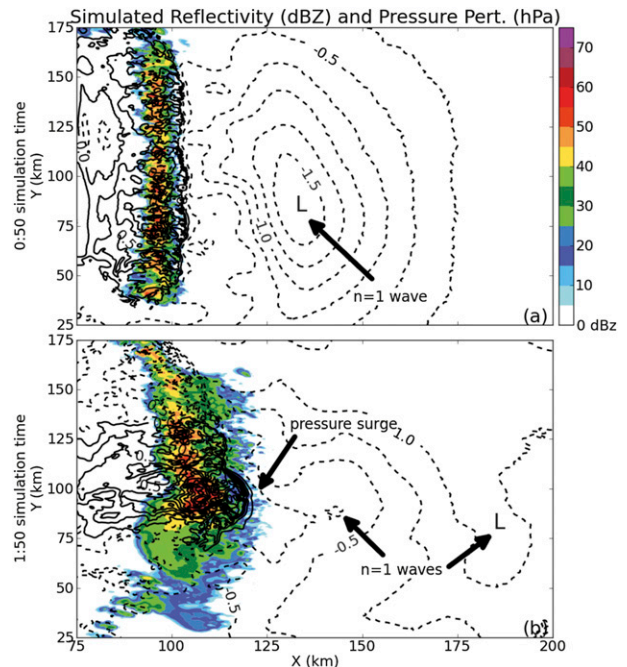


FIG. 6. Simulated reflectivity (filled contours, dBZ) and pressure perturbation (black, 0.25 hPa, negative dashed) at the lowest staggered model level, 50 m, for (a) 0050 and (b) 0150 simulation time. Black arrows point to the  $n = 1$  waves and pressure surge discussed in sections 4 and 5, respectively.

The vertical structure of this low pressure anomaly is displayed in Fig. 7. At simulation time 0050, in Figs. 7a and 7b, it is located at approximately  $x = 130$  km, where a low pressure perturbation in the lower half of the atmosphere is overlaid by a high pressure perturbation aloft. (The convective line is at 105 km.) Subsidence is indicated in the “eastern” half of the low pressure anomaly, and ascending motion in the “western” half. A temporary warming in the potential temperature field (Fig. 7b) is collocated with the pressure perturbations, due to the adiabatic warming and cooling associated with the downdraft–updraft couplet. The environmental flow toward the system is strengthened from the surface to 6 km aloft, and the flow away from the system is also intensified, at 6 km and above (Fig. 7b). In sum, this feature appears very similar to a gravity wave generated by a sudden increase, shortly followed by a decrease, of an  $n = 1$  heating profile (Nicholls et al. 1991).

By 0135 simulation time, the low pressure anomaly is at approximately  $x = 225$  km (Fig. 7c). The “widening” of the wave is largely due to the wave being advected slightly northward; the  $x$  cross section of the figure views the wave at an angle. (The updraft and downdraft portions of the wave also move at slightly different speeds.) Taking into account the mean tropospheric wind speed in direction of wave motion ( $-13.0$  m s $^{-1}$ ) and the translation

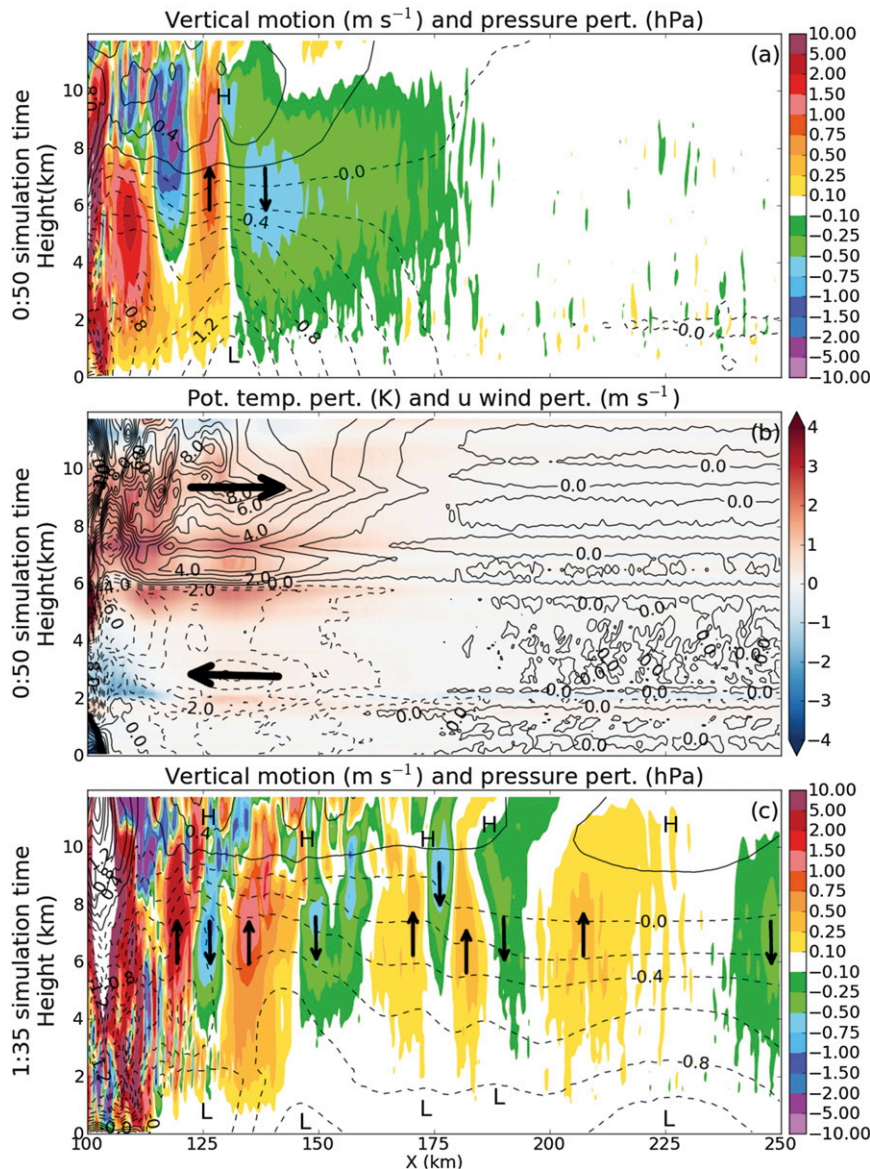


FIG. 7. Vertical  $x$  cross sections from 0 to 12 km, through the low pressure anomaly, averaged 5 km about the  $x$  cross section ( $y = 100.5\text{--}105.5$  km). (a) Vertical wind speed (color,  $\text{m s}^{-1}$ ) and pressure perturbation (black, 0.2 hPa, negative dashed) at 0050 simulation time. Upward and downward motion are indicated by arrows, and high and low pressure perturbations by letters H and L. (b) Potential temperature perturbation (color, K) and  $u$ -wind perturbation (black,  $1 \text{ m s}^{-1}$ , negative dashed) at 0050 simulation time. Inflow and outflow indicated by arrows. (c) As in (a), but for 0135 simulation time. The wave in (a) and the rightmost wave in (c) are the same feature.

speed of the domain ( $12.5 \text{ m s}^{-1}$ ), the modeled wave speed is an estimated  $32 \text{ m s}^{-1}$ . This is very close to the estimated first observed feature speed of  $32.5 \text{ m s}^{-1}$  (Fig. 4a). Using the  $N$  of the prestorm environment in the simulation,  $7.8 \times 10^{-3} \text{ s}^{-1}$ , and 12 km as the depth of the troposphere, (1) predicts the speed of an  $n = 1$  wave in this environment to be  $29.8 \text{ m s}^{-1}$ . This is somewhat

slower than both the modeled and observed speeds, but still very similar.

Also evident in Fig. 7c are four other features, at  $x = 120, 145, 175,$  and  $182$  km, that appear very much like  $n = 1$  gravity waves. To determine if these features are also waves generated by surges in the  $n = 1$  heating profile, a Hovmöller diagram of vertical motion at 6 km

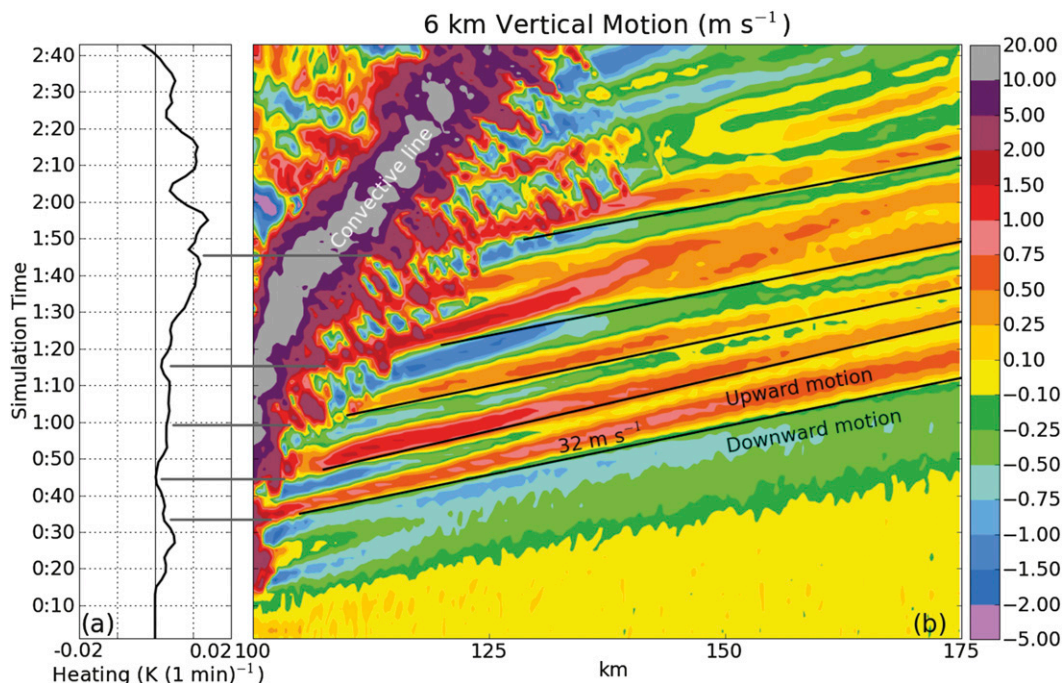


FIG. 8. (a) Mean microphysical heating [ $\text{K (1 min)}^{-1}$ ] between 5.2 and 7.3 km aloft,  $y = 100.5\text{--}105.5$  km as in Fig. 7, and across the entire domain in the  $x$  direction, from 0000 to 0300 simulation time. (b) Time evolution of horizontal distribution of vertical motion ( $\text{m s}^{-1}$ ) at 6 km aloft, averaged 5 km about the  $x$  cross section. Signatures of the five gravity waves discussed in section 4, and shown in Fig. 7c, are denoted by black lines. Gray lines connect the time of initial generation of these waves to the heating rate at the same time.

was created (Fig. 8b). A height of 6 km was selected as it is half the height of the troposphere and vertical motion associated with an  $n = 1$  wave should be strongest there (Nicholls et al. 1991); this is observed in Fig. 7a. The mean microphysical heating between 5.2 and 7.3 km, the closest three vertical levels above and below 6 km, was also calculated (Fig. 8a). This was calculated along a 5-km  $y$  cross section through the  $n = 1$  wave pressure responses ( $y = 100.5\text{--}105.5$  km, shown in Fig. 7) and over the entire domain in the  $x$  direction. It should be noted that the heating rates shown are averages over an area and therefore of small magnitude. It is possible that cells within that area have larger heating fluctuations.

From Fig. 8, it can be seen that changes in the mean midlevel heating rate correspond well with changing-amplitude signatures in the vertical motion field. For example, an increase in heating between approximately simulation time 0022 and 0028 produces an area of subsidence that propagates away from the source. The decrease in heating between simulation time 0029 and 0033 generates an area of ascent that does the same. This process is repeated numerous times throughout the simulation; as an illustration the five waves shown in Fig. 7c are marked on Fig. 8b by thin black lines. The times of generation of each of these waves, as determined by first

visibility of the wave signature within the vertical motion field, are connected to the heating rate at the same time by thin gray lines. Each upward motion response occurs in conjunction with a decrease in the midlevel heating rate, although the decrease at simulation time 0100 is small. The variations in the heating rate appear regular or even quasi periodic, similar to the periodic convective development noted in Lane and Zhang (2011).

Figures 9a–e show in gray the mean microphysical heating profile, over the same cross section as Fig. 8a, at the time of generation of each of these fast-moving responses of upward motion. Heating through almost the entire depth of the troposphere is evident in each, typical of an  $n = 1$  wave mode superimposed with one or more higher-order modes associated with low-level cooling. The profiles in black are from times shortly before wave generation; each upward motion response is associated with a decrease in heating throughout the midlevels. This decrease corresponds to a decrease in the amplitude of the  $n = 1$  mode of heating.

The waves generating the vertical motion perturbations all propagate at approximately the same speed,  $32 \text{ m s}^{-1}$ . This speed is very similar to the speed of all four pressure features tracked across Oklahoma in Figs. 4a–d. Perturbations in pressure similar to those observed in

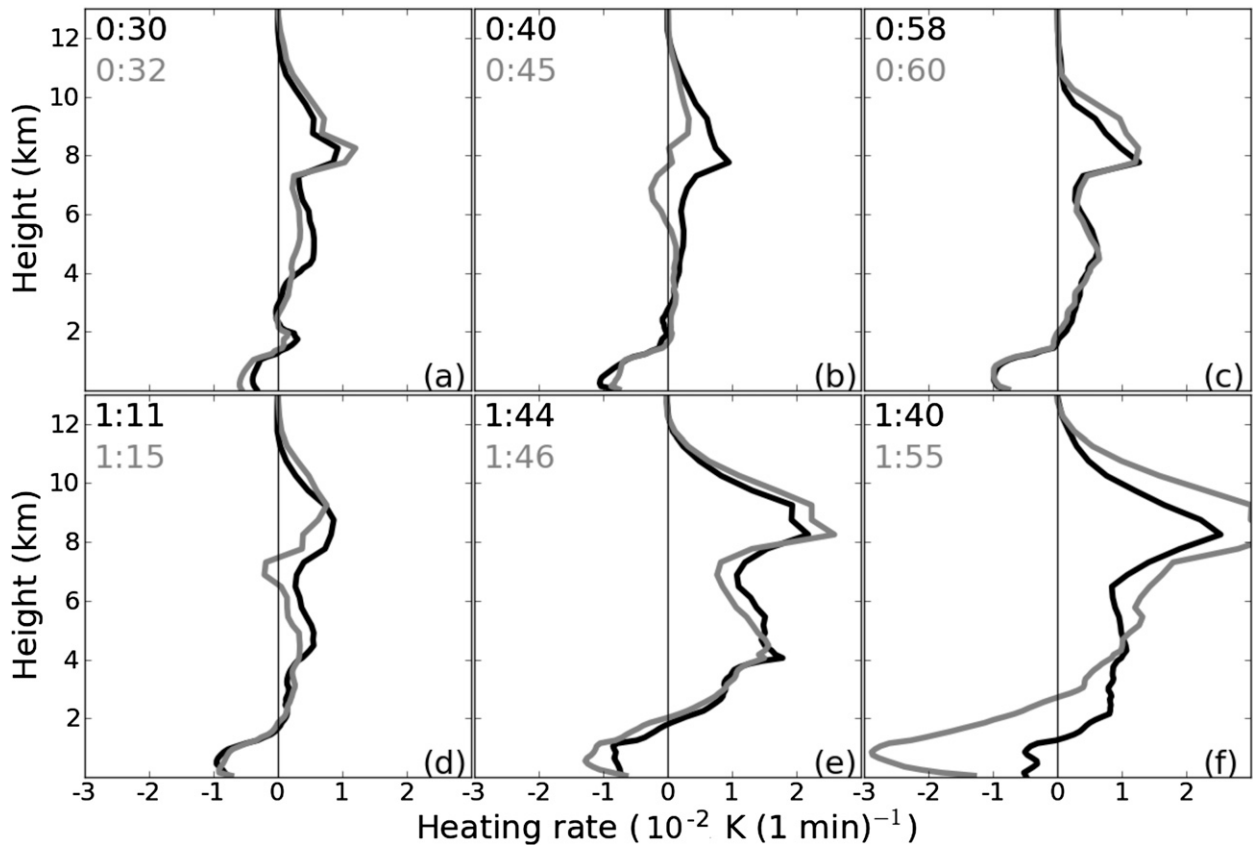


FIG. 9. Mean microphysical heating profiles [ $1 \times 10^{-2} \text{ K (1 min)}^{-1}$ ] between  $y = 100.5$  and  $105.5$  km (5 km about pressure surge) and across the entire domain in the  $x$  direction. (a)–(e) Gray lines show the heating profile at the time of wave generation (waves shown in Fig. 8); black lines are the profiles from shortly before generation. (f) The heating profiles shortly before (black) and at the time of (gray) development of the pressure surge gravity wave. Times of each profile are noted in each subfigure.

Fig. 3 are also evident in the simulated surface pressure (not shown). Therefore, it is a reasonable assumption that these observed features were reflections at the surface of  $n = 1$  gravity waves generated by variations in the convective heating profile.

Lane and Reeder (2001) found that the subsidence generated by an  $n = 1$  wave due to an increase in heating decreased the prestorm convective available potential energy (CAPE) in their study by approximately  $240 \text{ J kg}^{-1}$ , or 15% of the ambient environmental value. Conversely, the wave produced due to a decrease in the first internal mode of heating should lift, cool, and moisten the troposphere, increasing the CAPE. Figure 10 displays the CAPE over the same horizontal cross section as Fig. 8, with respect to time. As expected, the variations in CAPE very closely match the gravity waves shown in Fig. 8b.

The first  $n = 1$  wave front passage produced the largest variation in CAPE, a decrease of  $270 \text{ J kg}^{-1}$  from 0020 to 0035 simulation time at  $x = 110$  km. With each subsequent gravity wave passage, the CAPE values vary approximately  $200 \text{ J kg}^{-1}$ , or about 6%–8% with respect

to the initial sounding CAPE of  $3294 \text{ J kg}^{-1}$ . This is somewhat less than the Lane and Reeder (2001) results, but their simulations used a more stable atmosphere, with an  $N$  of  $0.0115 \text{ s}^{-1}$ , as opposed to this study's  $0.0078 \text{ s}^{-1}$ ; higher potential temperature perturbations are expected with increased stability. The convective inhibition values (not shown) do not vary significantly after passage of the first  $n = 1$  wave; even the effects of that wave are small, on the order of  $3 \text{ J kg}^{-1}$ . Because the largest magnitudes of vertical motion associated with each  $n = 1$  wave were located at approximately 6 km, and most of the CIN was located in the 0–3-km layer, the lack of effect on CIN is not surprising. Most of the CAPE variations were due to changes in the midlevel lapse rate around these peak vertical motions.

## 5. Pressure surge

### a. Feature description

A surge of higher pressure ahead of the convective line can be seen in Fig. 6b, in the same location where

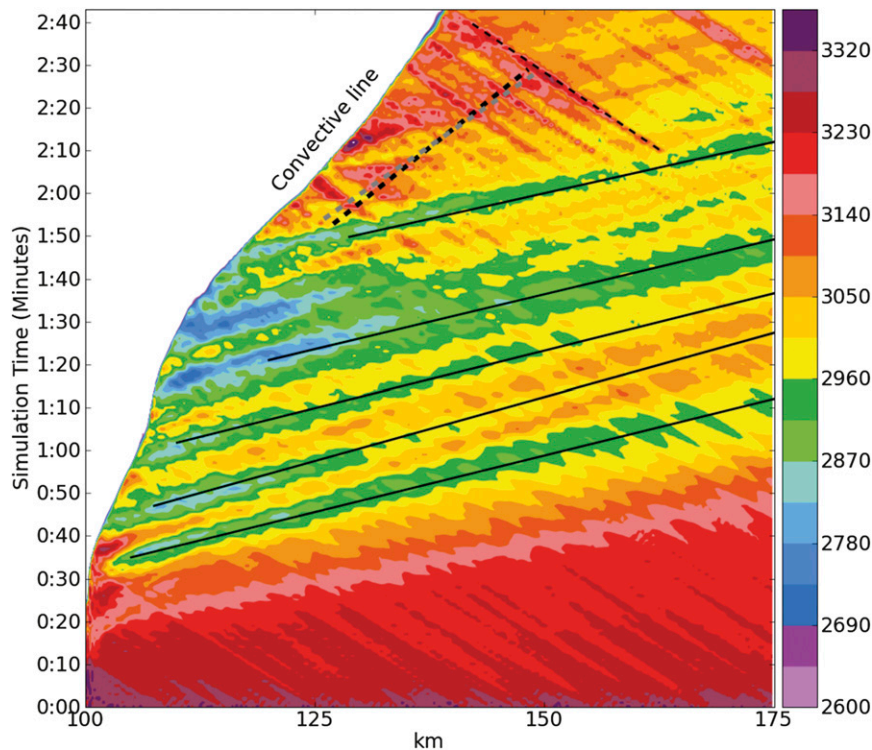


FIG. 10. Time evolution of horizontal distribution of CAPE (color,  $45 \text{ J kg}^{-1}$ ), averaged 5 km about the  $x$  cross section as in Fig. 8b. Five thin black lines track the five gravity waves discussed in section 4 and shown in Fig. 7. Thick dashed gray and black lines denote the pressure surge discussed in section 5. The thin dashed black line tracks a cloud generated by a high-frequency gravity wave, discussed in section 6.

the convective line was beginning to bow. (Also evident are additional  $n = 1$  waves.) As discussed above, the observed pressure surge extended approximately 20 km ahead of the convective line. The surge in Fig. 6b extends approximately 5 km ahead of the convective line and will later extend as far as 12 km ahead of the convective line, but both of these are a shorter distance than observed. The bowing portion of the simulated convective line was much shorter than observed as well—approximately 25 km in length instead of 100 km, meaning that associated cooling would be of smaller size as well. However, the simulated heating time series and associated  $n = 1$  waves match very well with the observed pressure perturbations, as discussed in the previous section. Thus, it is not unreasonable to expect the processes generating the simulated surge to be similar to those generating the observed surge.

Figure 11 displays a vertical cross section through the surge immediately after its development. A positive pressure perturbation (with respect to the initial state) ahead of the convective line, between  $x = 120$  and 125 km and reaching vertically to 2 km, is evident. The general trend of pressure increasing toward the convective line

continues from  $x = 132$  km, however. The prestorm pressure field has been significantly modified by the numerous  $n = 1$  wave features already propagating ahead of the convective line. Overall, the net effect of these earlier waves was a decrease in surface pressure ahead of the system. Thus, within Fig. 11 the general trend of increasing pressure is more relevant than absolute positive or negative perturbations, and the pressure surge will be identified here as the increasing pressure gradient from  $x = 120$  to 132 km, from 0 to 2.5 km aloft.

A number of higher-frequency features are also noticeable in the cloud water and vertical motion fields in Fig. 11, between  $x = 125$  and 150 km and at approximately 2 km and 5 km aloft. These features will be discussed in section 6. Unfortunately, because these higher-frequency features were in the same area as the pressure surge, the surge's exact structure and evolution were difficult to determine.

To better examine the pressure surge another Hovmöller diagram, of surface pressure along the same cross section through the surge, was constructed (Fig. 12b). Because the peak microphysical cooling occurred at 0.85 km, the mean microphysical heating

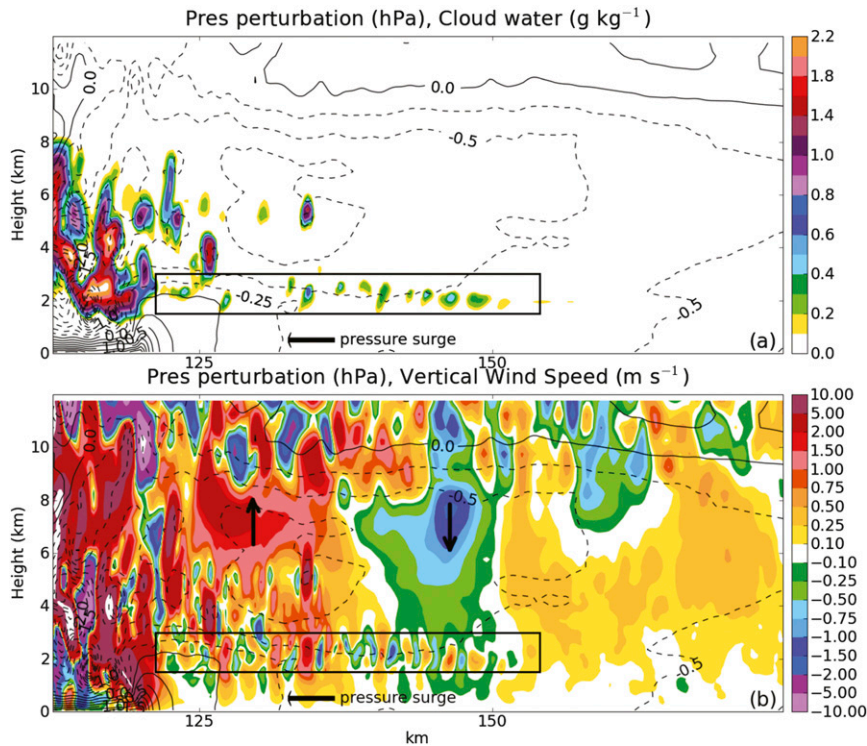


FIG. 11. Vertical  $x$  cross sections from 0 to 12 km, through the low pressure anomaly, averaged 5 km about the  $x$  cross section. (a) Vertical wind speed (color,  $\text{m s}^{-1}$ ) and pressure perturbation (black, 0.2 hPa, negative dashed) at 0050 simulation time. Upward and downward motion indicated by arrows, and high and low pressure perturbations by letters H and L. (b) Potential temperature perturbation (color, K) and  $u$ -wind perturbation (black,  $1 \text{ m s}^{-1}$ , negative dashed) at 0050 simulation time. Inflow and outflow indicated by arrows. (c) As in (a), but for 0135 simulation time. The wave in (a) and the rightmost wave in (c) are the same feature.

near that level (0.85 km) was examined and is displayed in Fig. 12a. Evident within Fig. 12b are a number of compression waves, propagating at approximately  $360 \text{ m s}^{-1}$ , causing periodic oscillations within the surface pressure and heating fields. As these oscillations are strongest at the surface and do not appear above 4 km, propagate horizontally only, and do not have any associated vertical velocity perturbations, the waves appear to be Lamb waves (Nicholls and Pielke 2000; Fanelli and Bannon 2005). CM1 is a compressible model (Bryan and Fritsch 2002) so this type of behavior is expected and was formally evaluated by Smith and Bannon (2008).

The five waves noted in Fig. 7c also appear in Fig. 12b as low pressure regions propagating away from the convective line (marked by thin black lines). Not every  $n = 1$  wave that is visible in Fig. 8b is also evident at the surface. Because of variations in tropospheric wind shear and stability, not all vertical levels of a gravity wave travel at the same speed (Bretherton 1966; Tulich et al. 2007). The first  $n = 1$  wave has the strongest surface pressure response. The subsidence associated with that

wave lasts for the longest time period (Fig. 8b), resulting in the low surface pressures.

Immediately prior to the appearance of the pressure surge, at approximately 0143 simulation time, a strong increase in 0.85-km cooling is evident in Fig. 12a. The cause and vertical structure of the cooling will be discussed later, but its timing in relation to the pressure surge is unmistakable. The surge cannot be a bore because there is not a sufficient density discontinuity between the surface layer and the layer above (Fig. 5). The pressure surge is also moving faster than the convective line and associated gravity current, which has a speed of  $7.6 \text{ m s}^{-1}$  during the same period and is labeled in Fig. 12b. The pressure surge and gravity current are clearly unique features in Fig. 12b and are separated by approximately 10 km at 0225 simulation time. Thus, the evidence suggests that the pressure surge feature is a gravity wave generated by increased cooling in the lower levels of the convective line.

From Fig. 11, the leading edge of the pressure surge can be delineated by the  $-0.25$ -hPa contour. However, because of the oscillations in the low-level pressure field

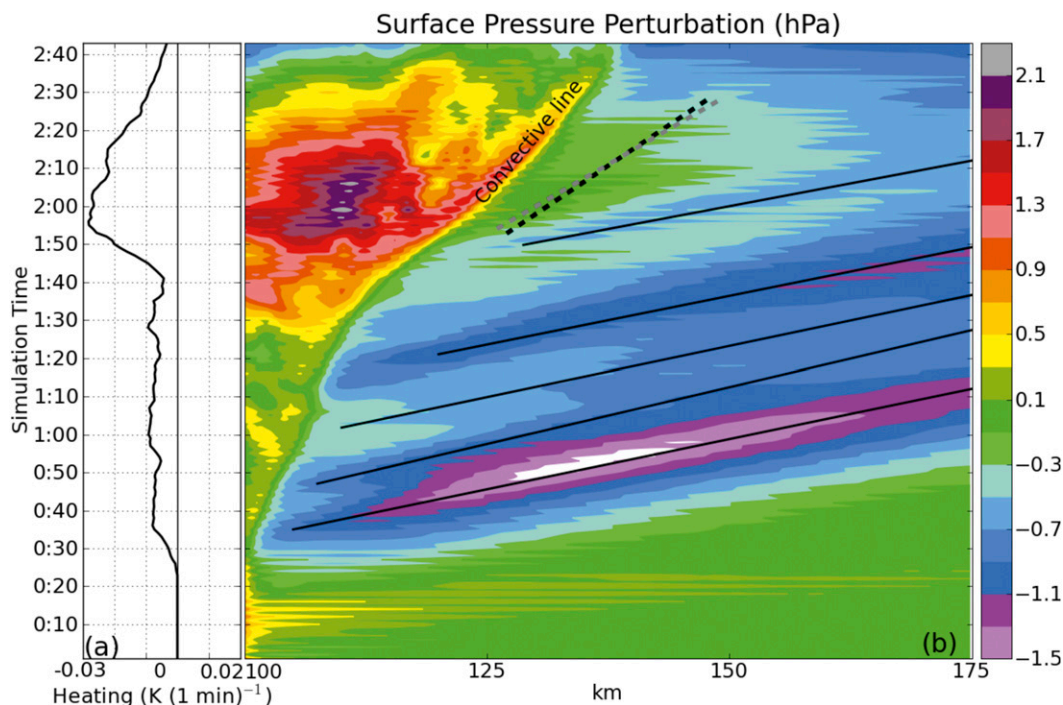


FIG. 12. (a) Mean microphysical heating [ $\text{K (1 min)}^{-1}$ ] between 0.65 and 1.05 km aloft,  $y = 100.5\text{--}105.5$  km (5 km about pressure surge), and across the entire domain in the  $x$  direction. (b) Time evolution of surface pressure perturbation (hPa) averaged 5 km about the  $x$  cross section. Thin black lines are as in Fig. 8b. The thick dashed black and gray lines show the progression of the pressure surge feature.

due to Lamb waves, tracking the surge using this contour does not produce a constant speed. Evaluation of Fig. 12b shows fluctuations in surface pressure with a period of approximately 1 min. Thus, to minimize the error introduced by these fluctuations, two speeds of the surge-leading  $-0.25\text{-hPa}$  contour were calculated: one from 0153 to 0229 simulation time, and the other from 0154 to 0228, using 2-min intervals within these periods.

The two calculated speeds are displayed in Fig. 12b as gray and black dashed lines, and they are very similar:  $11.3$  and  $9.8\text{ m s}^{-1}$ , respectively. After calculating the mean speed and removing the domain translation and mean wind in direction of surge motion, this yields a feature speed of  $11.0\text{ m s}^{-1}$ . Figure 9f shows an increase in low-level cooling immediately prior to the surge extending to 4 km. Using (1) and the  $N$  calculated immediately in front of the system at that time ( $7.7 \times 10^{-3}\text{ s}^{-1}$ ), the predicted speed for a wave generated by cooling extending to 4 km is  $9.8\text{ m s}^{-1}$ . The two speeds agree reasonably well, particularly considering the possible error added to the speed estimation by the Lamb and high-frequency waves.

HJ00 observed similar gravity wave behavior in response to a moving source of cooling. In their section 3b, a two-dimensional cooling source extending to 4 km was

prescribed to move at  $10\text{ m s}^{-1}$  in a linear numerical model. The cooling produced a gravity wave response moving at  $13\text{ m s}^{-1}$ , or  $3\text{ m s}^{-1}$  ahead of the cool source. The response contained a positive pressure perturbation extending to approximately 3 km aloft, overtopped by a weak low pressure perturbation (see their Fig. 5b). Because the cool source and wave speed were similar, the positive surface pressure perturbation was amplified by over 20% compared to a similar simulation with a stationary cooling source. As the speed of the pressure surge gravity wave and convective line are also similar in this simulation, it is possible the pressure surge response is being enhanced by this effect.

In Lane and Reeder (2001), the heating profile generating an  $n = 3$  wave extended to the tropopause and contained three antinodes consisting of low- and upper-level cooling and midlevel warming. The resulting pressure perturbations combined to extend the depth of the troposphere as well. In HJ00, the wave response was produced solely by low-level cooling, and the pressure response also remained in the lower levels. The pressure responses in both studies appeared very similar at lower levels, at least at time scales on the order of 2 h or less; at longer time scales, the vertical propagation of the wave in HJ00 became evident. The pressure surge gravity

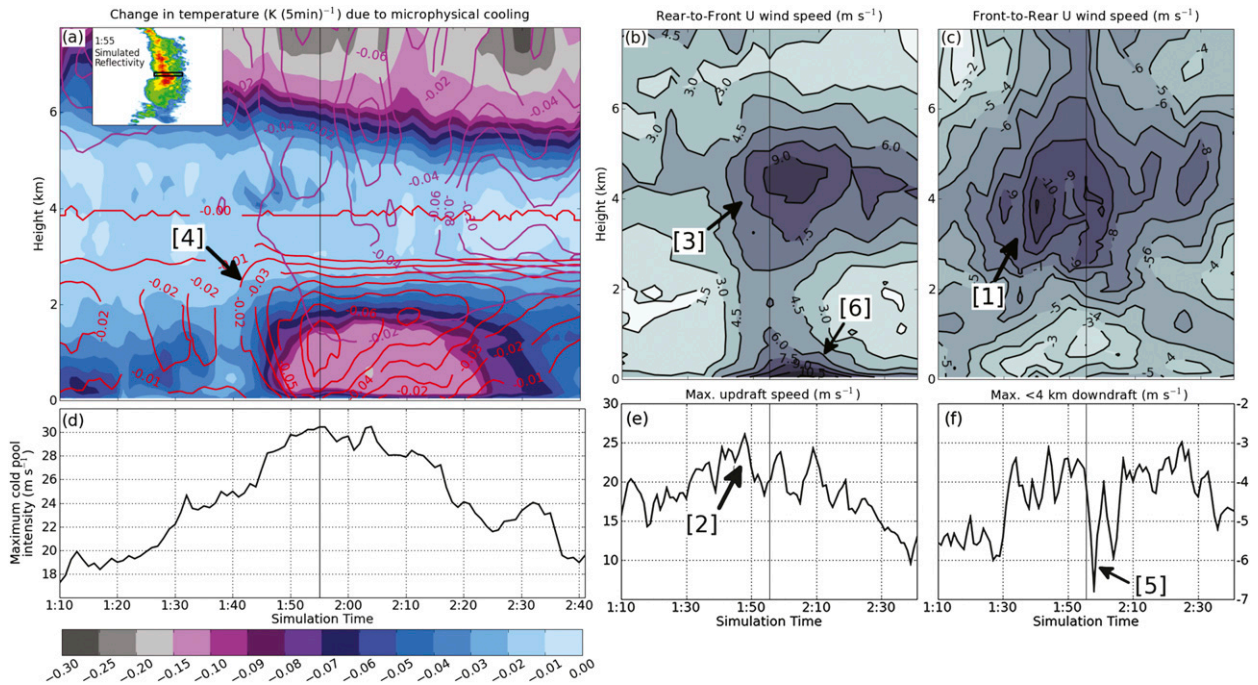


FIG. 13. Time–height series of mean vertical profiles, created by averaging over the horizontal width of the system and pressure surge in the  $x$  direction, and 5 km about the pressure surge and bow echo in the  $y$  direction. Area averaged over shown in inset in (a); area moves with convective line. The positive and negative  $u$ -wind averages were calculated separately. The thin black vertical line in each is the time of the start of the pressure surge. (a) Microphysical cooling rates due to evaporation [filled contours,  $\text{K} (5 \text{ min})^{-1}$ ], melting [red,  $0.01 \text{ K} (5 \text{ min})^{-1}$ ], and sublimation [purple,  $0.02 \text{ K} (5 \text{ min})^{-1}$ ]. (b) Storm-relative front-to-rear  $u$  wind ( $1.5 \text{ m s}^{-1}$ ). (c) Storm-relative rear-to-front  $u$  wind ( $1 \text{ m s}^{-1}$ ). (d) Maximum cold pool intensity ( $C$ ,  $\text{m s}^{-1}$ ). (e) Maximum upward vertical motion ( $1 \text{ m s}^{-1}$ ). (f) Maximum downward vertical motion ( $1.0 \text{ m s}^{-1}$ ). Labels (arrows) 1 through 6 detail the bowing process and are discussed in the text.

wave response appears to be produced solely by the low-level cooling. Examination of the Scorer parameter for a wave speed of  $11 \text{ m s}^{-1}$  (not shown, but very similar to Fig. 17) shows a trapping level around 2 km, which acts to trap the wave energy associated with the surge in the lower levels. A pressure surge gravity wave produced in a simulation with that trapping layer removed reached above 4 km.

The pressure surge observed in ASJ10 moved at a speed of  $21.6 \text{ m s}^{-1}$ , which is significantly faster than seen in the simulation. However, a few factors must be considered. The stability and mean wind of the environment through which the observed pressure surge was propagating is not known. Only the ground-relative speed of the observed surge was calculated. A mean environmental wind speed in the direction of the surge of  $10.6 \text{ m s}^{-1}$ , a not implausible value, would mean the actual surge wave speed was  $11.0 \text{ m s}^{-1}$ , what was simulated here. The observed surge could also have been generated by deeper low-level cooling than was simulated; through (1) this would result in a faster wave. Nevertheless, this simulation still provides a feasible mechanism that can generate the pressure

surge ahead of the bowing convective line seen so often by ASJ10.

#### b. Low-level cooling source

The cause of the sudden increase in the low-level cooling can be seen in the time–height cross sections shown in Fig. 13. These are mean vertical profiles created at each output time by averaging over the horizontal width of the convective system and pressure surge in the  $x$  direction, and 5 km about the pressure surge in the  $y$  direction. (Averaging area is shown in the inset in Fig. 13a; this area travels with the convective line). The positive and negative  $u$  wind averages are calculated separately. Model grid points are separated into two groups, one containing points with rear-to-front flow and the other with front-to-rear flow. The mean horizontal motion of each group is calculated and displayed separately in Figs. 13b and 13c. This procedure allows examination of mean fields without the opposing fields canceling each other out. The magnitude of the intensity of the cold pool  $C$  is shown in Fig. 13d, and it is calculated using  $C^2 = \int_0^h B dz$ , where  $B$  is buoyancy and  $h$  the height at which  $B$  becomes 0. The value of  $B$  is given by

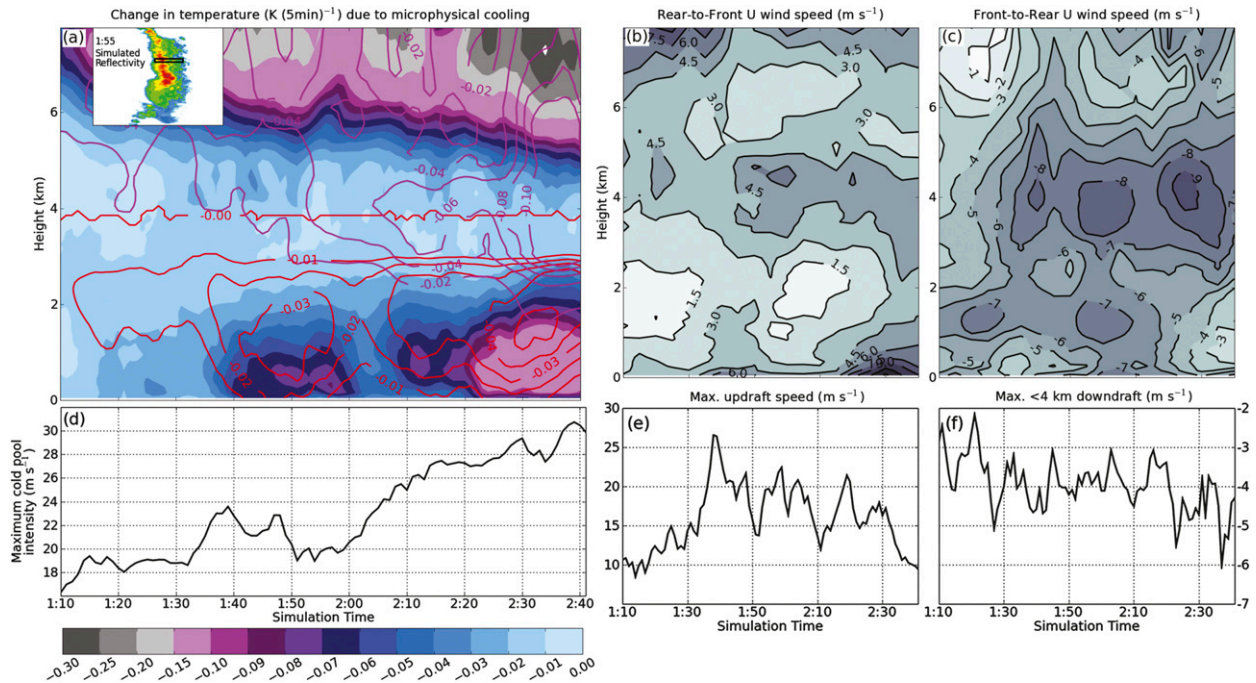


FIG. 14. As in Fig. 13, but for a nonbowing segment of the convective line, shown in inset in (a).

$$B = g \left[ \frac{\theta - \bar{\theta}}{\bar{\theta}} + 0.61(q_v - \bar{q}_v) - q_t \right], \quad (3)$$

where  $g$  is gravitational acceleration,  $\theta$  potential temperature,  $q_v$  water vapor mixing ratio, and  $q_t$  total hydrometeor mixing ratio; the bars designate environmental conditions. The maximum updraft speed and maximum low-level (below 4 km) downdraft speed are shown in Figs. 13e and 13f.

Initially, the storm-relative front-to-rear flow increases at 0130 simulation time, at approximately 3.5 km aloft (arrow 1 in Fig. 13c). Shortly thereafter, the convective updraft suddenly strengthens as well (arrow 2 in Fig. 13e). The midlevel rear-to-front flow also shows a strong increase at this time, and it deepens up to 6 km and extends to the surface (arrow 3 in Fig. 13b). Following this, at 0145 simulation time, a large increase in all three of the microphysical cooling fields (arrow 4 in Fig. 13a) occurs immediately prior to the appearance of the pressure surge.

The sudden influx of dry air into the rear of the storm as indicated by Figs. 5 and 13b, as well as the descent of the rear-to-front flow to the surface (Fig. 13b), led to these large increases in evaporation and melting. The vertical extent of the total cooling by evaporation, melting, and sublimation at this time is approximately 4 km (Fig. 13a). Cold pool intensity significantly increases at this same time (Fig. 13d). Finally, at the simulation time the surge can be seen ahead of the convective line, 0155, the

convective downdraft suddenly strengthens even further (arrow 5 in Fig. 13f) and strong outflow appears at the surface (arrow 6 in Fig. 13b).

It is unclear at this time what causes the first increase in midlevel front-to-rear flow at simulation time 0130. However, after this point the sequence of events is what would be expected in new bowing development (Weisman 1992, 1993; Weisman and Rotunno 2005; James et al. 2006). The convective updraft strengthens, increasing heating aloft and strengthening the midlevel pressure perturbation. This forces an increase in the rear-to-front flow, bringing drier air into the system and aiding in evaporative and sublimation cooling. The increase in microphysical cooling helps intensify the low-level downdrafts. All of these in combination act to locally speed one portion of the convective line, creating a bow; the surface winds increase as well. A gravity wave, shown at the surface by a surge in increasing pressure, is produced by the strong increase in low-level cooling and travels ahead of the bowing segment of the convective line.

Time–height cross sections through a nonbowing section of the convective line at  $y = 125$  km, generated in the same manner as Fig. 13, are shown in Fig. 14. At simulation time 0130, the storm-relative front-to-rear inflow is approximately  $2 \text{ m s}^{-1}$  slower (Fig. 14c) than in the bowing segment. Convective updraft speeds at this time are weaker (Fig. 14e), and reduced updraft magnitudes are found in the lower levels (not shown). Significantly, after simulation time 0140 the mean rear-to-front flow at 4 km

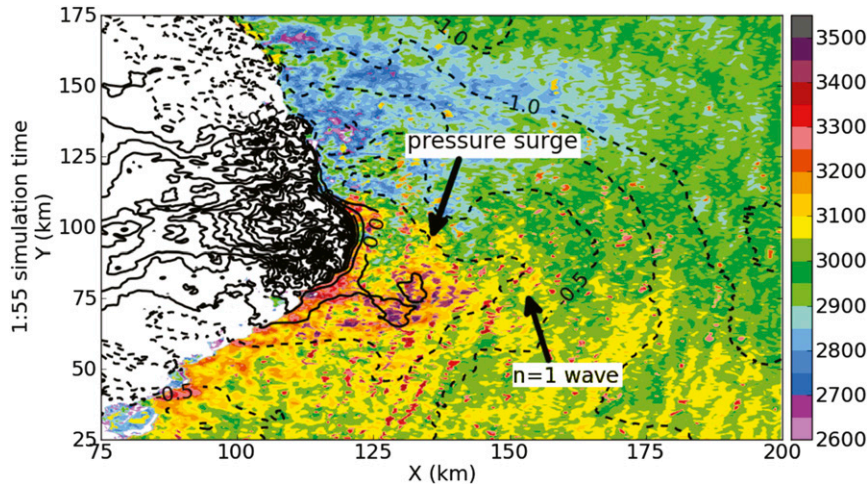


FIG. 15. CAPE (color,  $\text{J kg}^{-1}$ ) and pressure perturbation (black, 0.5 hPa, negative dashed) at 0155 simulation time.

is almost half the magnitude of the rear-to-front flow in the bowing segment (Fig. 14b), resulting in a reduced influx of dry air into the rear of the storm system.

As a result, the amount of microphysical cooling by melting and evaporation (Fig. 14a) is only half the amount seen in the bowing segment (Fig. 13a). The cold pool itself is also not as strong (Fig. 14d), resulting in a slower speed for this portion of the convective line compared to the bowing portion. Without a strong increase in cooling, the resulting gravity wave and surface pressure response are much weaker, and the pressure surge is not seen ahead of this portion of the convective line (Fig. 6b). Low-level downdrafts are also not as strong (Fig. 14f).

As the cooling (including sublimation) within the bowing segment generating the pressure surge gravity wave extends to 4 km (Figs. 13a, 9f), the lifting on its leading edge should also. Unfortunately, the signal of this vertical motion is masked by the high-frequency features (Fig. 11). A low-pass Lanczos filter (Duchon 1979) with cutoff wavelength at 4 km, approximately the horizontal wavelength of the high-frequency features, was applied horizontally to this cross section. Unfortunately artificial features are introduced in the vertical motion field by the filtering, particularly in the region near the convective line with its highly varying vertical motions. However, there does appear to be a signal in the filtered 0.85-km vertical motion field associated with the pressure surge gravity wave of upward (downward) motion on its leading (trailing) edge (not shown); HJ00 noted a similar low-level vertical motion response to a moving cool source.

Examination of the 0.85-km filtered potential temperature and water vapor perturbation fields reveals

signals of cooling and moistening on the leading edge of the surge gravity wave, and warming, but no drying, on the trailing edge, although these features were difficult to distinguish from artificial features introduced by the filtering process (not shown). These temperature perturbations are also similar to those observed by HJ00. The lack of drying on the trailing edge was due to the additional moistening by high-frequency features noted in the next section. In Figs. 10 and 15 an approximate  $250 \text{ J kg}^{-1}$  increase in the unfiltered CAPE field is evident over the same area as the surge, from 3050 to 3300  $\text{J kg}^{-1}$ . The CAPE increase appears to be collocated with the warming without drying on the trailing edge of the surge wave, although this is difficult to determine because of the artificial noise due to the filtering. In any event, the pressure surge is associated with a nonnegligible increase in CAPE, and there is not an increase of similar magnitude along other, nonbowing portions of the convective line without a pressure surge (Fig. 15).

Surprisingly, CIN was minimally affected by the pressure surge gravity wave (not shown). The main signal shown in the CIN field was a result of the high-frequency features, discussed in section 6.

### c. Effect of pressure surge on updraft strength

The increase in presystem CAPE associated with the pressure surge gravity wave should theoretically result in an increase in convective updraft strength. However, because convective updraft strength is also dependent on the tilt of that updraft, connecting variations in the maximum updraft speed to variations in presystem CAPE is not simple. As updraft tilt increases, the convective updraft weakens due to downward motion incited by a stronger, downward-directed pressure gradient (Parker 2010). The

tilt of the updraft is typically determined by the ratio of  $C$  to the low-level environmental storm-relative shear ( $\Delta u_{\text{env}}$ ) where a ratio of 1 is considered an upright updraft (Rotunno et al. 1988; Weisman and Rotunno 2004; Bryan et al. 2006). However, Weisman (1992) noted the importance of the rear inflow jet in determining updraft tilt, instead using the following ratio:

$$\frac{C^2 - u_j^2}{\Delta u_{\text{env}}^2} = \frac{C_j^2}{\Delta u_{\text{env}}^2}, \quad (4)$$

where  $u_j^2$  is defined as  $(u_H^2 - u_0^2)$ ,  $u_H$  is the storm-relative flow within the system at the height of the cold pool, and  $u_0$  is the flow at the surface.

To better evaluate the effect of increases in CAPE on updraft speed, the tilt of the updraft at the time must be determined. The ratio given in (4),  $C_j^2/\Delta u_{\text{env}}^2$ , was calculated for both the bowing and nonbowing segments of the convective line. This ratio was selected instead of  $C/\Delta u_{\text{env}}$  because of obviously strong rear-to-front flow associated with this system (Figs. 13b, 14b), and the importance of rear-to-front flow in bow echoes (Weisman 1993). The time series of  $C_j^2/\Delta u_{\text{env}}^2$  are displayed in Fig. 16a. Also,  $u_H$  and  $u_0$  were calculated at the point of maximum  $C$  in the cross section, and  $\Delta u_{\text{env}}$  was the 0–2.5-km shear; in this case almost all shear was confined below 2.5 km.

Because of the increased cooling and cold pool intensity after simulation time 0140 in the bowing segment of the convective line,  $C_j^2/\Delta u_{\text{env}}^2$  increases significantly (Fig. 16a), even reaching values above 15 immediately after the pressure surge. Such a value suggests a very tilted updraft (Weisman 1992; Bryan et al. 2006). In addition to the intense cold pool, the rear-to-front flow within the bowing segment descends to the surface farther behind the convective line after simulation time 0140 (not shown). A large negative value of  $u_j^2$  results, also tilting the updraft farther rearward over the cold pool (Weisman 1992). The updraft in the nonbowing segment is more upright, with smaller  $C_j^2/\Delta u_{\text{env}}^2$  values (Fig. 16a) due to a less intense cold pool (Fig. 14d) and slower surface-based rear-to-front flow (Fig. 14b). Based on this information alone, the convective updraft within the bowing segment would be expected to be weaker than its nonbowing counterpart during this time period.

However, the bowing segment updraft is stronger than the updraft in the nonbowing segment, particularly from simulation time 0155 to 0200 and from 0205 to 0210 (Fig. 16b), during and shortly after the generation of the pressure surge gravity wave. The increased CAPE generated by the pressure surge and high-frequency gravity waves aids in producing these stronger updraft magnitudes, despite the increased tilting of the updraft. The

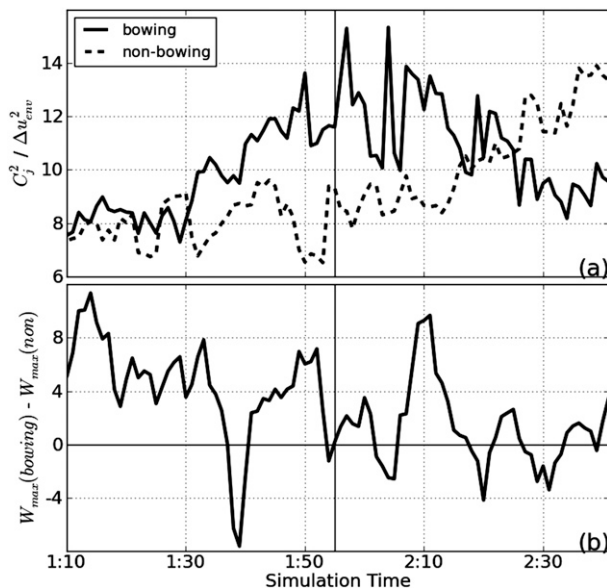


FIG. 16. (a)  $C_j^2/\Delta u_{\text{env}}^2$  for cross sections through the pressure surge and bowing convective line (solid) and through  $y = 125$  km, a nonbowing segment of the convective line (dashed). (b) Difference between maximum convective updraft in the bowing and nonbowing segments of the convective line. Thin black vertical line in both indicates time pressure surge first appeared ahead of the convective line.

magnitude of the CAPE ahead of the nonbowing segment is not as large (Fig. 15), and the associated updraft is not as strong (Fig. 14e) during the same time period.

## 6. High-frequency gravity waves

In Fig. 11b, a series of updraft–downdraft couplets are located between approximately 2 and 2.5 km aloft, and between  $x = 125$  and 150 km. Couplets of this nature are noted at this height as early as 30 min into the simulation. Within the updraft portion of these couplets condensation regularly occurs and clouds form (Fig. 11a). These features appear remarkably similar to those observed in Fovell et al. (2006) in association with high-frequency gravity waves generated by multicellularity in the convective line. While the speed of these features varied, an average speed at the time of the pressure surge is estimated at  $-3.6 \text{ m s}^{-1}$ ; this is an actual phase speed of  $6.5 \text{ m s}^{-1}$  once the mean wind at that level ( $2.4 \text{ m s}^{-1}$ ) and the domain translation ( $12.5 \text{ m s}^{-1}$ ) is accounted for.

Unlike the low-frequency gravity waves discussed above, these higher-frequency waves require a trapping level other than the tropopause so their energy does not propagate vertically immediately. In Fovell et al. (2006), the trapping level was provided by the curvature of the wind profile due to outflow aloft at anvil level. However, the vertical motions associated with the high-frequency

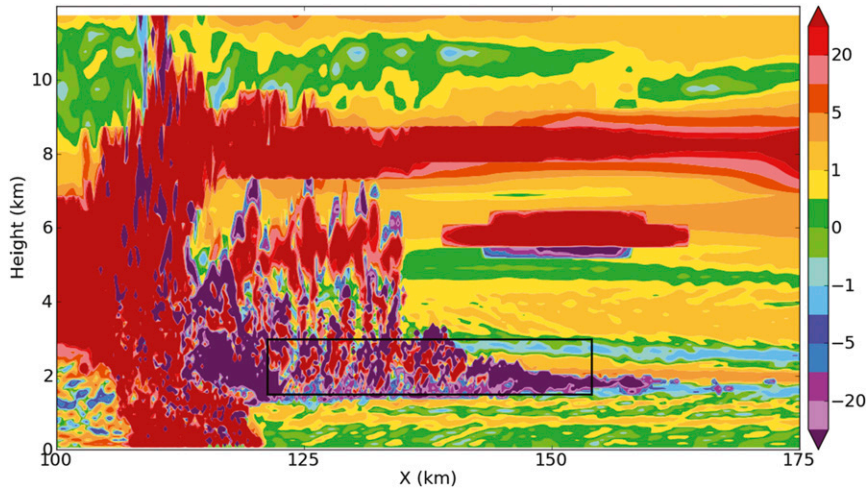


FIG. 17. Vertical 0–12-km cross section at 0155 simulation time, averaged 5 km about the  $x$  axis, of the Scorer parameter (color,  $1 \times 10^{-6} \text{ m}^{-2}$ ) for a wave speed of  $6.5 \text{ m s}^{-1}$ . Black box delineates the same area as in Fig. 11.

gravity waves in that study extended to 7 km. Here, the couplets are trapped in a layer around 2 km.

An examination of the environmental stability explains this (Fig. 17). The Scorer parameter was calculated as in Fovell et al. (2006), as

$$l^2 = \frac{N_m^2}{(U - c)^2} - \frac{\partial^2 U / \partial z^2}{(U - c)}, \quad (5)$$

where  $N_m^2$  is the Brunt–Väisälä frequency, calculated separately for saturated and subsaturated air as discussed in section 1,  $U$  is ground-relative wind speed,  $z$  is height, and  $c$  is the average high-frequency ground-relative wave speed,  $6.5 \text{ m s}^{-1}$ . A thin stable layer is evident between approximately 2 and 2.5 km. Both above and below this layer are regions where the Scorer parameter is negative, which act to reflect the wave energy. Thus, the updraft couplets and associated clouds remain in the 2–2.5-km layer. A similar trapping level is also evident just below 6 km (Fig. 17), with updraft–downdraft couplets and cloud development immediately below (Fig. 11). A simulation was run with the trapping levels around 2 km removed, and no high-frequency wave features were found in that region. High-frequency waves were still found just below 6 km, as that trapping level was unmodified.

It was also noted by Fovell et al. (2006) that these high-frequency gravity waves can have an effect on the prestorm environment, particularly when condensation occurs within an associated updraft and forms a cloud. The latent heat released would act to modify the parcel’s stability; if ingested into the storm the extra warmth and moisture would intensify the system. However, if the cloud became large enough to produce rain, it could

create its own cold pool, which would instead have a negative effect when ingested. In this case, none of the clouds produced rain or had individual cold pools, so the feedback to the system should be positive. The effect of the latent heat release on the stability of the 2–2.5-km layer can be seen within Fig. 17 between  $x = 125$  and 130 km: the latent heat release from the formation of multiple clouds, and the turbulent mixing associated with this, mixed out the stable layer and decreased the overall stability.

Increases in CAPE due to these small clouds can be seen in Fig. 15. The magnitude of these increases is largest within the pressure surge: small cells containing CAPE values larger than  $3500 \text{ J kg}^{-1}$  can be seen immediately ahead of the convective line within the pressure surge in Fig. 15. This effect can also be seen in Fig. 10. One specific cloud (and associated increase in CAPE) is tracked in Fig. 10 by a thin dashed black line. The formation of the cloud was associated with increased CAPE (approximately  $200 \text{ J kg}^{-1}$ ) and decreased CIN (approximately  $2 \text{ J kg}^{-1}$ ; not shown). However, within the CAPE field (Fig. 10) the variations associated with these high-frequency features appear largest in magnitude, by approximately  $50 \text{ J kg}^{-1}$ , after passage of the pressure surge gravity wave.

As in Fovell et al. (2006), the low-frequency wave “prepares” the environment for later high-frequency features by gently lifting of its leading edge the lower levels of the troposphere. This allows the later high-frequency features to generate much stronger variations in CAPE by forming clouds in this newly moistened layer. Once a cloud is formed due to lifting from the high-frequency wave, it does not travel with the wave but

instead is advected by the mean flow at that level. Within Fig. 10, the thin dashed line is used to track the speed of one of the clouds at  $-11.4 \text{ m s}^{-1}$ . Accounting for the  $12.5 \text{ m s}^{-1}$  domain translation, the cloud moves at the speed of the mean wind at that level. It is advected toward the system as in Fovell et al. (2006). Small clouds forming immediately ahead of, and then being overtaken by, the convective line were detected by the KTLX Weather Surveillance Radar-1988 Doppler (WSR-88D) from 0516 through 0635 UTC (not shown).

## 7. Conclusions

A number of surface pressure features observed by Adams-Selin and Johnson (2010) in conjunction with the 13 March 2003 bow echo over Oklahoma are further evaluated, using both additional examination of the observations and a high-resolution numerical model simulation. The observed surface pressure features include one approximately 2-hPa temporary decrease in pressure that propagates quickly away from the convective line at  $32.5 \text{ m s}^{-1}$ , followed by a subsequent rise, dip, and rise in pressure. These pressure perturbations propagate away at approximately the same speed. Also observed is a surge of increasing pressure ahead of the convective line. Pressure surges of this nature were observed in 35 of 39 bow echoes examined by Adams-Selin and Johnson (2010). The surges generally occurred immediately prior to or at the same time as the bow echo developed.

A numerical simulation is performed to understand the processes generating these features. In the simulation, numerous gravity waves are generated by the evolving heating profile. Fluctuations in the amplitude of deep convective heating generate  $n = 1$  gravity wave responses that travel quickly away from the convective line, as theorized by Nicholls et al. (1991). An increase in the heating results in a wave with subsidence throughout the tropospheric column and corresponding warming and drying with a low surface pressure perturbation; a decrease in that profile results in a wave with ascent throughout the column, and subsequent cooling and moistening with a high surface pressure perturbation.

Not only do the modeled  $n = 1$  waves propagate at nearly the same speed as the observed fast-moving low pressure feature ( $32$  and  $32.5 \text{ m s}^{-1}$ , respectively), but the vertical structure of the modeled feature matches theoretical studies (Nicholls et al. 1991) exactly. Thus, it is concluded that the observed fast-moving pressure features are indeed  $n = 1$  gravity waves. Wave generation is also very frequent and associated with fluctuations in the  $n = 1$  heating profile. Eighteen  $n = 1$  waves are produced just in this 2.6-h simulation, and surface

reflections of four  $n = 1$  waves are noted in the observations. Within the simulation, each  $n = 1$  wave modifies the prestorm CAPE profile by between 6% and 8% of the initial CAPE value.

A surge of increasing pressure occurs ahead of the bowing segment of the convective line as bowing develops. This simulated pressure feature propagates at a speed of approximately  $11.0 \text{ m s}^{-1}$ , in good agreement with a gravity wave postulated to be excited by strong low-level cooling extending to 4 km with a speed of  $9.8 \text{ m s}^{-1}$ . Shortly prior to surge development, the system's front-to-rear inflow and convective updraft increases within this segment, strengthening the midlevel pressure perturbation, and resulting in an increase in rear-to-front flow. This increases low-level microphysical cooling and convective downdrafts up to 4 km by introducing additional dry air; the cooling generates the gravity wave. An approximate  $250 \text{ J kg}^{-1}$  increase in CAPE, or 8% of the initial sounding, is noted in conjunction with the combination of the pressure surge and other higher-frequency features, suggesting that lifting and moistening is occurring at lower levels. This higher CAPE partially explains the increasing strength of the convective updraft in the bowing segment at time of bowing, despite increased updraft tilt due to a strengthening cold pool and surface-based rear-to-front flow.

The larger magnitudes of rear-to-front flow and low-level microphysical cooling rates, generation of the gravity wave and pressure surge, and resulting higher presystem CAPE are all confined to the bowing segment of the convective line and the area immediately in advance of it. A nonbowing convective segment was examined, which exhibits rear-to-front flow and low-level microphysical cooling rates of half the magnitude of those in the bowing segment. The convective updraft strength at time of bowing was also weaker, despite a less pronounced updraft tilt.

The appearance of the pressure surge can be explained in the context of Haertel and Johnson (2000) wherein the linear response to a moving low-level cool source was investigated. In that study it was found that when the gravity wave speed associated with the vertical scale of the cooling approximately matched the speed of the cool source, an amplification of the surface pressure response occurred. The modeling results here are analogous.

Finally, a number of high-frequency features, updraft-downdraft couplets that produced small clouds, are trapped in the 2–2.5-km stable layer in advance of the system. These features are similar to those modeled by Fovell et al. (2006), although in this case they are trapped by a much lower unstable layer as opposed to the curvature of the wind profile due to the outflowing anvil aloft. The latent heat release associated with the clouds

that form within the updraft portion of each wave modifies the prestorm stable layer by decreasing its stability and the environmental CIN, and increasing the CAPE. However, these effects are more noticeable after passage of the pressure surge. The gentler lifting generated by that low-frequency wave moderately moistens the lower troposphere, allowing larger destabilizing effects to be generated by the high-frequency features. The results support the mechanisms described by Fovell et al. (2006).

The results herein have multiple implications for current convective modeling. As has already been noted in other studies (Lane and Reeder 2001), these types of gravity waves have a significant effect on the prestorm environment. However, in this study waves are continually generated by both strengthening and weakening of the convective heating profile. Wave fronts generated in response to a weakening of the amplitude of the  $n = 1$  heating profile had not been previously observed except in theory (Nicholls et al. 1991). Each passage of just one of these waves significantly modifies the prestorm environment, making characterization of the prestorm environment even more difficult than previously supposed.

The lifting and subsequent destabilization created by the pressure surge gravity wave, and associated increase in updraft strength, positively feed back to the system, helping it further intensify as the bowing process occurs. This indicates that the gravity waves generated by a system can have a feedback effect of short time scales. An interesting point is that this simulated bow echo had not yet produced large amounts of stratiform precipitation. Typically higher vertical wave modes are associated with melting and evaporation in the stratiform region; this case shows that such a profile can be created within the convective region alone.

The importance of low-level cooling in generation of new bowing development is underscored by this study, particularly as Adams-Selin and Johnson (2010) observed this pressure surge feature in conjunction with many developing bow echoes. As rear-to-front flow and convective downdrafts are key in producing the low-level cooling seen here, the characteristics of the source of these flows—the ambient environmental conditions—are of consequence. Furthermore, these simulated cooling rates highly depend on the chosen microphysical parameterization. This highlights the significance of correctly parameterizing microphysical processes when simulating bow echo development, which is still an area of active work.

*Acknowledgments.* This research was supported by National Science Foundation Grants ATM-0500061 and AGS-0966758. Oklahoma Mesonet data were provided through the courtesy of the Oklahoma Mesonet, a

cooperative venture between Oklahoma State University and the University of Oklahoma and supported by the taxpayers of Oklahoma. The WSI NOWrad data were provided by the Mesoscale and Microscale Meteorology Division of the University Corporation for Atmospheric Research (UCAR) through David Ahijevych. Computing resources were provided by the Navy Department of Defense Supercomputing Resource Center (Navy DSRC) and the Army Research Laboratory Department of Defense Supercomputing Resource Center (ARL DSRC), which are sponsored by the DoD High Performance Computing Modernization Program. The authors thank Susan van den Heever and Russ Schumacher of CSU, and Morrison Weisman of UCAR, for many discussions regarding this work. We also thank George Bryan for assistance in using the CM1 model. Patrick Haertel aided with data interpretation of the Oklahoma Mesonet data. The comments of three anonymous reviewers were greatly appreciated.

#### REFERENCES

- Adams-Selin, R. D., and R. H. Johnson, 2010: Mesoscale surface pressure and temperature features associated with bow echoes. *Mon. Wea. Rev.*, **138**, 212–227.
- Bretherton, C. S., and P. K. Smolarkiewicz, 1989: Gravity waves, compensating subsidence and detrainment around cumulus clouds. *J. Atmos. Sci.*, **46**, 740–759.
- Bretherton, F. P., 1966: The propagation of groups of internal gravity waves in a shear flow. *Quart. J. Roy. Meteor. Soc.*, **92**, 466–480.
- Bryan, G. H., and J. M. Fritsch, 2002: A benchmark simulation for moist nonhydrostatic numerical models. *Mon. Wea. Rev.*, **130**, 2917–2928.
- , and R. Rotunno, 2009: The maximum intensity of tropical cyclones in axisymmetric numerical model simulations. *Mon. Wea. Rev.*, **137**, 1770–1789.
- , and M. D. Parker, 2010: Observations of a squall line and its near environment using high-frequency rawinsonde launches during VORTEX2. *Mon. Wea. Rev.*, **138**, 4076–4097.
- , J. C. Knievel, and M. D. Parker, 2006: A multimodel assessment of RKW theory's relevance to squall-line characteristics. *Mon. Wea. Rev.*, **134**, 2772–2792.
- Duchon, C. E., 1979: Lanczos filtering in one and two dimensions. *J. Appl. Meteor.*, **18**, 1016–1022.
- Fanelli, P. F., and P. R. Bannon, 2005: Nonlinear atmospheric adjustment to thermal forcing. *J. Atmos. Sci.*, **62**, 4253–4272.
- Fovell, R. G., 2002: Upstream influence of numerically simulated squall-line storms. *Quart. J. Roy. Meteor. Soc.*, **128**, 893–912.
- , G. L. Mullendore, and S. H. Kim, 2006: Discrete propagation in numerically simulated nocturnal squall lines. *Mon. Wea. Rev.*, **134**, 3735–3752.
- Gallus, W. A., Jr., and R. H. Johnson, 1991: Heat and moisture budgets of an intense midlatitude squall line. *J. Atmos. Sci.*, **48**, 122–146.
- Haertel, P. T., and R. H. Johnson, 2000: The linear dynamics of squall line mesohighs and wake lows. *J. Atmos. Sci.*, **57**, 93–107.
- , —, and S. N. Tulich, 2001: Some simple simulations of thunderstorm outflows. *J. Atmos. Sci.*, **58**, 504–516.

- Houze, R. A., Jr., 1982: Cloud clusters and large-scale vertical motions in the tropics. *J. Meteor. Soc. Japan*, **60**, 396–410.
- James, R. P., J. M. Fritsch, and P. M. Markowski, 2006: Bow echo sensitivity to ambient moisture and cold pool strength. *Mon. Wea. Rev.*, **134**, 950–964.
- Johnson, R. H., and G. S. Young, 1983: Heat and moisture budgets of tropical mesoscale anvil clouds. *J. Atmos. Sci.*, **40**, 2138–2147.
- , and B. E. Mapes, 2001: Mesoscale processes and severe convective weather. *Severe Convective Weather, Meteor. Monogr.*, No. 50, Amer. Meteor. Soc., 71–122.
- Klemp, J. B., 1994: On the dynamics of gravity currents in a channel. *J. Fluid Mech.*, **269**, 169–198.
- Knupp, K., 2006: Observational analysis of a gust front to bore to solitary wave transition within an evolving nocturnal boundary layer. *J. Atmos. Sci.*, **63**, 2016–2035.
- Lane, T. P., and M. J. Reeder, 2001: Convectively generated gravity waves and their effect on the cloud environment. *J. Atmos. Sci.*, **58**, 2427–2440.
- , and M. W. Moncrieff, 2008: Stratospheric gravity waves generated by multiscale tropical convection. *J. Atmos. Sci.*, **65**, 2598–2614.
- , and F. Zhang, 2011: Coupling between gravity waves and tropical convection at mesoscales. *J. Atmos. Sci.*, **68**, 2585–2598.
- Liu, C., and M. W. Moncrieff, 2004: Effects of convectively generated gravity waves and rotation on the organization of convection. *J. Atmos. Sci.*, **61**, 2218–2227.
- Mapes, B. E., 1993: Gregarious tropical convection. *J. Atmos. Sci.*, **50**, 2026–2037.
- McAnelly, R. I., J. E. Nachamkin, W. R. Cotton, and M. E. Nicholls, 1997: Upscale evolution of MCSs: Doppler radar analysis and analytical investigation. *Mon. Wea. Rev.*, **125**, 1083–1110.
- Nicholls, M. E., 1987: A comparison of the results of a two-dimensional numerical simulation of a tropical squall line with observations. *Mon. Wea. Rev.*, **115**, 3055–3077.
- , and R. A. Pielke, 2000: Thermally induced compression waves and gravity waves generated by convective storms. *J. Atmos. Sci.*, **57**, 3251–3271.
- , —, and W. R. Cotton, 1991: Thermally forced gravity waves in an atmosphere at rest. *J. Atmos. Sci.*, **48**, 1869–1884.
- Pandya, R. E., and D. R. Durran, 1996: The influence of convectively generated thermal forcing on the mesoscale circulation around squall lines. *J. Atmos. Sci.*, **53**, 2924–2951.
- , —, and M. L. Weisman, 2000: The influence of convective thermal forcing on the three-dimensional circulation around squall lines. *J. Atmos. Sci.*, **57**, 29–45.
- Parker, M. D., 2008: Response of simulated squall lines to low-level cooling. *J. Atmos. Sci.*, **65**, 1323–1341.
- , 2010: Relationship between system slope and updraft intensity in squall lines. *Mon. Wea. Rev.*, **138**, 3572–3578.
- Rotunno, R., J. B. Klemp, and M. L. Weisman, 1988: A theory for strong, long-lived squall lines. *J. Atmos. Sci.*, **45**, 463–485.
- Schmidt, J. M., and W. R. Cotton, 1990: Interactions between upper and lower tropospheric gravity waves on squall line structure and maintenance. *J. Atmos. Sci.*, **47**, 1205–1222.
- Schumacher, R. S., 2009: Mechanisms for quasi-stationary behavior in simulated heavy-rain-producing convective systems. *J. Atmos. Sci.*, **66**, 1543–1568.
- Smith, J. W., and P. R. Bannon, 2008: A comparison of compressible and anelastic models of deep dry convection. *Mon. Wea. Rev.*, **136**, 4555–4571.
- Stensrud, D. J., M. C. Coniglio, R. P. Davies-Jones, and J. S. Evans, 2005: Comments on “‘A theory for strong long-lived squall lines’ revisited.” *J. Atmos. Sci.*, **62**, 2989–2996.
- Thompson, G., P. R. Field, R. M. Rasmussen, and W. D. Hall, 2008: Explicit forecasts of winter precipitation using an improved bulk microphysics scheme. Part II: Implementation of a new snow parameterization. *Mon. Wea. Rev.*, **136**, 5095–5115.
- Tulich, S. N., D. A. Randall, and B. E. Mapes, 2007: Vertical-mode and cloud decomposition of large-scale convectively coupled gravity waves in a two-dimensional cloud-resolving model. *J. Atmos. Sci.*, **64**, 1210–1229.
- Wakimoto, R. M., 1982: The life cycle of thunderstorm gust fronts as viewed with Doppler radar and rawinsonde data. *Mon. Wea. Rev.*, **110**, 1060–1082.
- Weisman, M. L., 1992: The role of convectively generated rear-inflow jets in the evolution of long-lived mesoconvective systems. *J. Atmos. Sci.*, **49**, 1826–1847.
- , 1993: The genesis of severe long-lived bow echoes. *J. Atmos. Sci.*, **50**, 645–670.
- , and R. Rotunno, 2004: “‘A theory for strong long-lived squall lines’ revisited.” *J. Atmos. Sci.*, **61**, 361–382.
- , and —, 2005: Reply. *J. Atmos. Sci.*, **62**, 2997–3002.
- , W. C. Skamarock, and J. B. Klemp, 1997: The resolution dependence of explicitly modeled convective systems. *Mon. Wea. Rev.*, **125**, 527–548.